ELSEVIER

Coordination Chemistry Reviews
219–221 (2001) 509–543

COORDINATION CHEMISTRY REVIEWS

www.elsevier.com/locate/ccr

Coupled electronic states in *trans*-$MCl_2(H_2O)_4^{n+}$ complexes (M: Ni^{2+}, Co^{2+}, V^{3+}, Cr^{3+}) probed by absorption and luminescence spectroscopy

Guillaume Bussière, Rémi Beaulac, Benoit Cardinal-David, Christian Reber *

Département de chimie, Université de Montréal, Montreal, Canada QC H3C 3J7

Received 11 September 2000; received in revised form 18 December 2000; accepted 16 January 2001

This paper is dedicated to Professor Barry Lever on the occasion of his 65th birthday

Contents

* Corresponding author. Tel.: +514-343-7332; fax: +514-343-7586..
E-mail address: reber@chimie.umontreal.ca (C. Reber).

PII: S0010-8545(01)00349-6

Abstract

The electronic spectra of *trans*-$MCl_2(X_2O)_4^{n+}$ complexes (M: Ni^{2+}, Co^{2+}, V^{3+}, Cr^{3+} and X: H, D) are analyzed in order to understand interactions between electronic states. We present detailed low-temperature polarized absorption spectra of single crystals. Spectra were measured over a large range, from near-infrared to UV, and they show several spectroscopic effects arising from interactions between electronic states. The lowest-energy electronic transition in $VCl_2(H_2O)_4^+$ consists of sharp weak bands between 950 and 1030 nm, well separated from the more intense spin allowed bands. Observed energy differences and the temperature dependence of the transition intensities lead to a quantitative characterization of the ground state splitting. The analogous $CrCl_2(H_2O)_4^+$ chromophore has a much smaller energy separation between its lowest energy spin forbidden transition and the first spin allowed band. We examine the effect of this difference on the resolved spectra and compare it to related transition metal complexes. The strongest interaction between electronic states occurs in $NiCl_2(H_2O)_4$, where the lowest energy singlet state is very close in energy to a spin allowed crystal field band, giving rise to intense vibronic patterns. Experimental spectra are analyzed quantitatively using the time dependent theory of spectroscopy and established crystal field and Jahn–Teller approaches.

Keywords: Absorption spectroscopy; Emission spectroscopy; Raman spectroscopy; Nickel complexes; Vanadium complexes; Chromium complexes; Cobalt complexes

1. Introduction

Effects arising from coupled electronic states are important to many areas of chemistry, especially for transition metal compounds, which have a rich electronic structure where many states can interact [1]. Intersystem crossings in transition metal compounds have been reported and were discussed qualitatively, but most often not quantitatively, by several authors in the past [2–6]. There are numerous experimental manifestations of coupling between electronic states, and we will present examples involving spin–orbit coupling, the Jahn–Teller effect and configu-

ration interaction. Our study is based on experimental low-temperature absorption and emission spectra of *trans*-$MCl_2(X_2O)_4^{n+}$ (M: V^{3+}, Cr^{3+}, Co^{2+}, Ni^{2+}; X: H, D) complexes. Spin–orbit coupling between electronic states of different multiplicity is present in all complexes, but the magnitude of the resulting spectroscopic effects depends strongly on parameters like the spin–orbit coupling constant, the energy difference between interacting states, their potential surfaces and the off-diagonal ligand field matrix element between the states. We compare quantitatively the spectroscopic consequences of spin–orbit interaction in a series of transition metal complexes with the *trans*-dichlorotetraaquo ligand environment.

Several spectroscopic investigations of the $MCl_2(H_2O)_4^{n+}$ chromophores are reported in the literature. McCarthy et al. [7,8] have extensively studied the absorption spectra of $Cs_2CrCl_5{\cdot}4H_2O$ and $Cs_3VCl_6{\cdot}4H_2O$. Spectroscopic studies of $CoCl_2(H_2O)_4{\cdot}2H_2O$ were reported by Ferguson [9], Ferguson and Wood [10], Joy and Fogel [11] and Pappalardo [12]. The only spectroscopic study on $NiCl_2(H_2O)_4{\cdot}2H_2O$ reported before 1998 is by Gieleßen [13], who has also studied a series of other complexes of divalent metals with this ligand sphere. His pioneering publication in 1935 predates most applications of quantum mechanical models to transition metal compounds. To our knowledge, no quantitative overall comparison of the spectra of *trans*-dichlorotetraaquo complexes has been published.

The time dependent theory of spectroscopy is used in order to quantitatively describe intersystem crossings in the title compounds. The calculation of absorption spectra by time dependent theory was established by Heller [14]. The application of the theory to transition metal complexes has been discussed in detail in previous publications [15,16]. We have developed an approach for $NiCl_2(H_2O)_4$ and extend it to all compounds discussed here [1]. In view of the good agreement between experimental and calculated spectra, it appears that time dependent theory is an essential tool to understand electronic spectra and electronic structure of transition metal compounds.

2. Experimental section

2.1. Nickel and cobalt complexes

Crystals of *trans*-$MCl_2(X_2O)_4{\cdot}2X_2O$ ($X = H$ or D, $M = Ni^{2+}$ or Co^{2+}) were obtained by slow evaporation of saturated solutions of MCl_2 in X_2O over several days (in a desiccator for D_2O). $NiCl_2(H_2O)_4{\cdot}2H_2O$ crystallizes as regular monoclinic green prisms [17]. The crystal used for spectroscopic measurements had clearly defined optical extinction directions, determined between crossed polarizers. The polarized low-temperature absorption spectra were measured with the light beam perpendicular to the *ab* crystallographic plane. The projection of the molecular Cl–Ni–Cl axis in this plane is parallel to the crystallographic *a* axis and perpendicular to the *b* axis. The crystal was oriented on an X-ray diffractometer and the axes which are parallel to the extinction directions were identified. The labels π and σ

refer to the orientation of the molecular Cl–M–Cl axis relative to the electric vector of polarized light. $CoCl_2(H_2O)_4 \cdot 2H_2O$ crystallizes as regular monoclinic mauve prisms. The crystals are strongly dichroic and appear orange with the electric vector perpendicular to the *b* axis and mauve with the vector parallel to the *b* axis [9]. The orientation of the unit cell with respect to the crystal faces was also crystallographically determined in order to define the π and σ polarizations. Our analysis of the polarization directions is confirmed by the literature studies on $CoCl_2(H_2O)_4 \cdot 2H_2O$ which is isostructural to the nickel(II) analog [17,18].

2.2. Vanadium and chromium complexes

Crystals of $Cs_3VCl_6 \cdot 4X_2O$ and $Cs_2CrCl_5 \cdot 4X_2O$ (X = H or D) were obtained by slow evaporation of saturated acidic solutions of CsCl and MCl_3 (XCl 2 M in X_2O, X = H or D, $M = V^{3+}$ or Cr^{3+}) over several days (in a desiccator for D_2O). $VCl_3 \cdot 6X_2O$ was prepared by hydrating (with H_2O or D_2O) anhydrous VCl_3. $CrCl_3 \cdot 6H_2O$ is available commercially and $CrCl_3 \cdot 6D_2O$ can be obtained by several recrystallizations in D_2O. Crystallographic studies confirm that these compounds contain the *trans*-$MCl_2(X_2O)_4^+$ chromophore [7,8,19–23]. Infrared spectroscopic measurements show that our deuterated compound contains less than 4% hydrogen. $Cs_3VCl_6 \cdot 4X_2O$ crystallizes as dark green rectangular prisms, with one side particularly longer than the others. These crystals had clearly defined optical extinction directions, parallel to the crystallographic axes, determined between crossed polarizers. The molecular Cl–V–Cl axis is parallel to the crystallographic *a* axis, which coincides with the short side of the crystals. $Cs_2CrCl_5 \cdot 4X_2O$ forms dark green, slightly dichroic crystals [7]. $Cs_2CrCl_5 \cdot 4X_2O$ crystallizes in the monoclinic space group $C2/m$ [21,22].

2.3. Spectroscopic instrumentation

Crystal thicknesses for absorption spectroscopy were between 0.5 and 5 mm. Low-temperature polarized spectra were measured with a Varian Cary 5E spectrometer equipped with a pair of Glan–Taylor polarizers. All spectra are corrected for the baseline of the instrument. The sample temperature was controlled with an Oxford Instruments CF-1204 helium gas flow cryostat. Raman spectra were measured using a Renishaw System 3000 Raman imaging microscope. The microscope was used to focus the laser light onto a spot approximately 1 μm in diameter and to collect the scattered light. Spectra were measured using four different excitation wavelengths: 782 nm (near-infrared (NIR) diode laser), 632.8 nm (HeNe), 514.5 and 488.2 nm (argon ion) and the appropriate Renishaw notch filters allowing us to obtain clean spectra down to 100 cm^{-1} from the excitation wavelength. Back scattering Raman intensities were detected using a Peltier cooled CCD detector.

Emission spectra were taken using two different apparatus. The most sensitive instrument between 400 and 1050 nm is the Renishaw 3000 Raman imaging microscope. The Raman system was equipped with an elbow objective to focus the laser on the sample and to collect the emitted light in the helium cryostat described

above. The measurements between 1050 and 1650 nm were made with a Hamamatsu R5509-72 (serial No. JE-0156) photomultiplier tube cooled with liquid nitrogen. The 488 and 514 nm lines of a Coherent Innova CR-12 ion argon laser with the appropriate interference filters were used as excitation sources.

Lifetime measurements were made using a Continuum Minilite II Q-switched Nd:YAG pulsed laser at 532 nm. Measurements between 650 and 800 nm were made with a Hamamatsu R4632 photomultiplier connected to an optically triggered (Thorlabs FDS100 Si photodiode) Tektronix TDS380 digital oscilloscope.

3. *trans*-$NiCl_2(H_2O)_4$

3.1. $NiCl_2(H_2O)_4 \cdot 2H_2O$

We have reported previously [1] that nickel(II) aquo and chloro complexes are ideal models for a comprehensive study of interactions between electronic excited states. In fact, the $NiCl_2(H_2O)_4$ chromophore has the energetically closest electronic excited states of different spin multiplicity in the $MCl_2(X_2O)_4^{n+}$ series reported here. The energy separations between the first spin forbidden and spin allowed transitions vary in the order: $V^{3+} > Cr^{3+} > Ni^{2+}$, Co^{2+}. An advantage of the nickel(II) electronic structure for quantitative theoretical modeling is that the problem can be reduced to an interaction between two electronic states. This simple model cannot be used quantitatively to analyze more complicated cases, for instance the spectrum of the cobalt(II) complex in the visible spectral region. This d^7 ion has half-integer J values and double group symmetry labels have to be used, leading to interactions between multiple electronic states, a situation that is hard to analyze quantitatively. Another characteristic of the nickel(II) system is the large matrix element between interacting states and the highest spin–orbit coupling constant λ of the metals studied here, as summarized in Table 1.

3.2. Spectroscopic results

The overall absorption spectrum of the $NiCl_2(X_2O)_4$ chromophore is presented in Fig. 1 and it shows three spin-allowed crystal field bands and two spin-forbidden transitions. The oscillator strengths for the spin allowed and the first spin-forbidden bands in the unpolarized spectrum are on the order of 5×10^{-6} (band at 13459 cm^{-1}) and 3.6×10^{-7} (14820 cm^{-1}), respectively [1]. The value for the allowed transition is in the usual range but the value for the forbidden band is quite high, leading to an abnormally low intensity ratio $I_{triplet}/I_{singlet}$ of 14. The main feature of this spectrum is the intense vibronic progression on the high-energy side of the middle band. This vibronic progression has a higher spacing than the ground state vibrational frequency of the totally symmetric nickel-aquo stretching mode. Such progressions are observed for many nickel(II) complexes in the $^3T_{1g}/^1E_g$ (O_h labels) region of the spectrum, where crossing between allowed and forbidden states occurs. For the $NiCl_2(H_2O)_4$ chromophore, the σ polarized spectrum has a simple

Table 1
Comparison of parameters relevant for intersystem crossings in $MCl_2(H_2O)_4^{n+}$ complexes

Chromophore symmetry of the coupled states (O_h point group)	Energy separation of the first forbidden and the closest allowed transition (between maxima) (cm^{-1})	Matrix element (coupling constant between the states) (cm^{-1})	Intensity ratio $I_{allowed}/I_{forbidden}$ of coupled spin–orbit sublevels	Relation between λ and ζ, λ value and percentage of the free ion value (cm^{-1} (%))	λ and ζ for the free ion (cm^{-1}) [63]
$NiCl_2(H_2O)_4$, $^3T_{1g}/^1E_g$	1344	$-\lambda\sqrt{6}$, 730	6.1 (A_{1g}/A_{1g}) [a], 2.8 (calculated)	$\lambda = -\zeta/2$, −298, 92	$\lambda = -324$, $\zeta = 648$
$CrCl_2(H_2O)_4^+$, $^2E_g/^4T_{2g}$	1979	$-3\lambda\sqrt{6}/\sqrt{5}$ [b], −187	95 (U/U) [a], 87 (calculated)	$\lambda = \zeta/3$, 57, 63	$\lambda = 91$, $\zeta = 273$
$VCl_2(H_2O)_4^+$, $^1T_{2g}/^3T_{2g}$	6687	$-\lambda\sqrt{6}$ [c], −233	1118 (T_{2g}/T_{2g}), 1275 (calculated)	$\lambda = \zeta/2$, 95, 91	$\lambda = 104$, $\zeta = 208$
$CoCl_2(H_2O)_4$, $^4T_{2g}/^2E_g$	4000	0	–	$\lambda = -\zeta/3$, −172, 96	$\lambda = -180$, $\zeta = 540$

[a] Error on experimental value is large due to the difficulty to separate the experimental spectrum into two bands.
[b] Highest possible value [5,43].
[c] For $^1T_{2g}$, it is 0 for ^1E_g [43].

vibronic progression while a doubled pattern appears in π polarization, as shown in Fig. 2. The members of the progression in the σ polarized spectrum are separated by $430 \pm 5\ cm^{-1}$. The same large separation is observed in π polarization, but each member is twinned with an average $75\ cm^{-1}$ separation, much smaller than the spacing of the progression. The weak vibronic peaks between 18000 and 19000 cm^{-1} involve vibrational modes of the aquo ligand.

The first allowed transition to $^3T_{2g}$ (O_h label) is in the near-infrared region, as shown in Fig. 3. Magnetic dipole zero phonon lines are observed between 5500 and 7000 cm^{-1} for $NiCl_2(D_2O)_4{\cdot}2D_2O$. Ferguson and Wood [10] have observed similar transitions for the isostructural $CoCl_2(D_2O)_4{\cdot}2D_2O$. For $NiCl_2(H_2O)_4{\cdot}2H_2O$ these origins are not clearly observed because they overlap with more intense vibrational water overtones.

The Raman spectra at room temperature and 83 K show no vibrational transition at 430 cm^{-1}. The vibrational energies observed in the low-temperature Raman spectrum are 532, 377 and 364 cm^{-1}. The signal at 364 cm^{-1} is attributed to the totally symmetric nickel–water stretching mode.

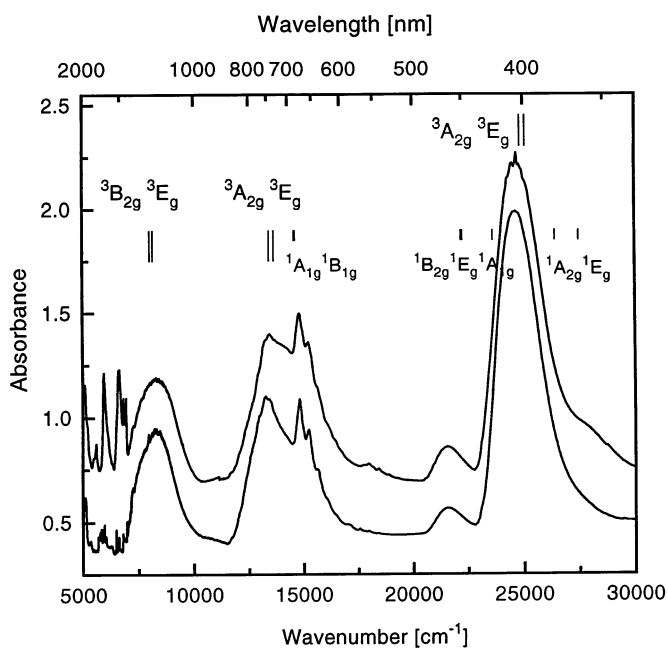

Fig. 1. Unpolarized absorption spectra of $NiCl_2(H_2O)_4{\cdot}2H_2O$ (top trace) and $NiCl_2(D_2O)_4{\cdot}2D_2O$ (bottom trace) at 5 K. The vertical lines represent the AOM energies calculated with parameters from Table 2 with $\zeta = 0$. The tall lines represent spin-allowed transitions, the short lines the spin-forbidden transitions.

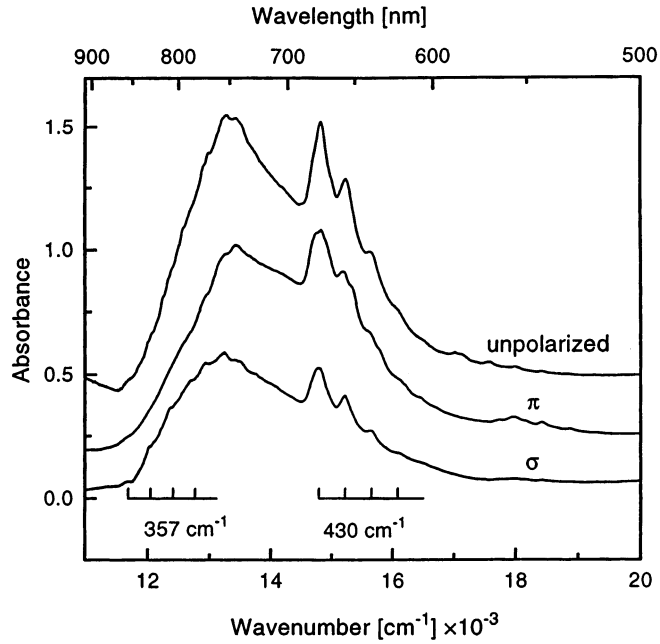

Fig. 2. Unpolarized spectrum of the $^3T_{1g}/^1E_g$ (O_h) region for $NiCl_2(D_2O)_4{\cdot}2D_2O$ (top trace) and polarized spectra of $NiCl_2(H_2O)_4{\cdot}2H_2O$ (bottom traces) at 5 K.

3.3. Intersystem crossing and vibronic structure in the absorption spectra: strong effects caused by spin–orbit coupling

We used idealized D_{4h} point group symmetry to analyze the polarized spectra of the *trans*-$NiCl_2(H_2O)_4$ chromophore. The region of the $^3T_{1g}/^1E_g$ (O_h) bands is of great interest and it is useful to use tetragonal symmetry to understand the features of this spectral region. In the D_{4h} point group, the ^1E_g (O_h) state is split into $^1A_{1g}$ and $^1B_{1g}$ levels. The $^3T_{1g}$ state separates into $^3A_{2g}$ and ^3E_g, which are then further split by spin–orbit coupling. The $^3A_{2g}$ state interacts only with the $^1A_{1g}$ state because there is no B_{1g} level among its spin–orbit components. This situation leads to a spectrum with a simple progression when the $^3A_{2g}$ state is involved in the transition and with a double progression when the ^3E_g state is involved. Considering the number of progressions observed and the fact that a transition to a doubly degenerate E_g level should have twice the oscillator strength of a transition to a non-degenerate A or B level, it is clear that in Fig. 2 the $^3A_{2g}$ state dominates the σ polarized spectrum while the ^3E_g state appears prominently in π polarization.

The angular overlap model (AOM) [30,31] was used in order to obtain the energetic order of triplet and singlet excited states in this tetragonal chromophore. The angular overlap parameters $e_\sigma(H_2O)$, $e_{\pi s}(H_2O)$ and $e_{\pi c}(H_2O)$ were estimated from the spin-allowed band maxima of $Ni(H_2O)_6(NO_3)_2$ at 5 K [1,24]. The corresponding absorption maxima of $NiCl_6^{4-}$ in $CsCdCl_3$, $CsMgCl_3$ [25,26] and

$NiCl_2$ [27,28] were used to determine e_σ(Cl) and e_π(Cl), respectively. We set the parameters $e_\sigma(H_2O)$ and $e_{\pi s}(H_2O)$ to 4000 and 1000 cm^{-1}, respectively, while e_σ(Cl) and e_π(Cl) are set to 3700 and 1000 cm^{-1}, respectively, for the *trans*-dichlorotetraaquo nickel(II) complex. We analyze the spectra of the divalent nickel and cobalt ions with AOM e_σ and e_π parameters as close as possible to these values. Bencini et al. [29] obtained mean values for $e_\sigma(H_2O)$ and $e_\pi(H_2O)$ of 3802 and 889 cm^{-1} (without π anisotropy) for divalent ions, summarized in their Table 5. The same authors report values for chloride ligands in their Table 2 for divalent ions; their averages are 4496 and 1581 cm^{-1} for e_σ(Cl) and e_π(Cl), respectively, in relatively good agreement with the values used here. For the trivalent chromium and vanadium complexes we set $e_\sigma(H_2O)$ and e_σ(Cl) to 7000 and 6000 cm^{-1}, respectively. Values of 7000 and 7500 cm^{-1} for $e_\sigma(H_2O)$ were suggested by Hitchman et al. [30] for $V(H_2O)_6^{3+}$, in agreement with the value used here. Hitchman et al. have also suggested that $e_{\pi c}(H_2O)$ should be quite small, on the order of 500 ± 500 cm^{-1} [30]. For all complexes, we set $e_{\pi c}(H_2O) < e_{\pi s}(H_2O)$, a condition consistent with a simple covalent model of the interaction between the water molecule and the metal ion where the p_x orbital of water does not contribute to the metal–ligand bonds because of its involvement in bonding to the hydrogen atoms [30,31]. For all AOM calculations we assume an angle $\psi = 0$, as the position of the hydrogen atoms is not known exactly for all title complexes. This assumption is justified in the case of

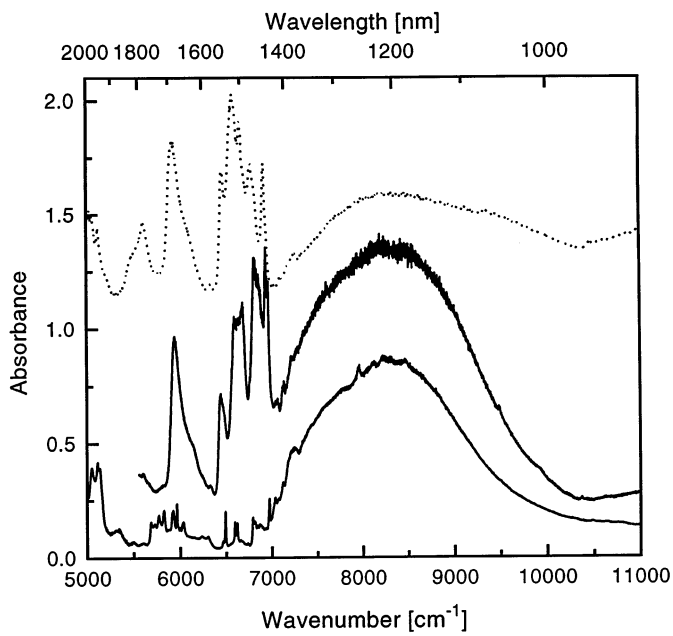

Fig. 3. First electronic transition to the $^3T_{2g}$ state for *trans*-$NiCl_2(H_2O)_4 \cdot 2H_2O$ (top trace) and for *trans*-$NiCl_2(D_2O)_4 \cdot 2D_2O$ (bottom trace). The dotted trace shows the same region for $CoCl_2(H_2O)_4 \cdot 2H_2O$ with the water overtones very similar to those of nickel(II) analog.

Table 2
Spectroscopic parameters and ligand field calculations for the title complexes

	Raman frequencies 83 K (cm^{-1})	Absorption 5 K (cm^{-1}) [{D_{4h}} O_h (ion)] ⟨polarization⟩	Calculated ligand-field energies [D_{4h} (spin–orbit)]	Emission 5 K (cm^{-1}) [D_{4h}]	Angular overlap parameters for ligand field calculations (cm^{-1})	
$NiCl_2(H_2O)_4 \cdot 2H_2O$	296	8279 [$^3T_{2g}$]	8000 [$^3B_{2g}$] [a]		$e_\sigma(H_2O)$ 4000	*B* 950
	364		8142 [^3E_g] [a]		$e_{\pi s}(H_2O)$ 1000	*C* 3800
	377	13 245 [{$^3A_{2g}$} $^3T_{1g}$] ⟨σ⟩	13 416 [$^3A_{2g}$] [a]		$e_{\pi c}(H_2O)$ 700	ζ 596
	548	13 430 [{^3E_g} $^3T_{1g}$] ⟨π⟩	13 634 [^3E_g] [a]		e_σ(Cl) 3700	
	701	14 803 [^1E_g]	15 233 [(A_{1g})] [b]		e_π(Cl) 1000	
		21 614 [$^1A_{1g}$, $^1T_{2g}$]	22 023 [(B_{2g})] [b]			
		24 691 [$^3T_{1g}$ (^3P)]	24 834 [$^3A_{2g}$] [a]			
			25 074 [^3E_g] [a]			
$Cs_2CrCl_5 \cdot 4H_2O$	150	13 629 [$^4T_{2g}$] [c]		12 121 [^4E_g]	$e_\sigma(H_2O)$ 7000	*B* 599
	228	14 438 [^2E_g]	14 438 [(Γ_6)] [b]	13 655 [^4E_g] [c]	$e_{\pi s}(H_2O)$ 1000	*C* 3332
	241	14 800 [?]	14 822 [(Γ_7)] [b]		$e_{\pi c}(H_2O)$ 500	ζ 171
	286	16 630 [$^4T_{2g}$]	16 401 [$^4E_{2g}$] [a]		e_σ(Cl) 6000	
	440		17 000 [$^4B_{2g}$] [a]		e_π(Cl) 1000	
	484	20 690 [{$^2B_{2g}$} $^2T_{2g}$]	21 650 [(Γ_7)] [b]			
	734	21 760 [$^4A_{2g}$ $^4T_{1g}$]	21 297 [$^4A_{2g}$] [a]			
		23 040 [^4E_g $^4T_{1g}$]	23 636 [^4E_g] [a]			
		35 130 [^4E_g $^4T_{1g}$]	35 948 [^4E_g] [a]			
			36 688 [$^4A_2$] [a]			
$Cs_3VCl_6 \cdot 4H_2O$			8 [$^3A_{2g}$ (E)] [b]		$e_\sigma(H_2O)$ 7000	*B* 622
			2443 [^3E_g] [a]		$e_{\pi s}(H_2O)$ 1150	*C* 2857
	169	9717 [$^1T_{2g}$]	9718 [(B_{2g})] [b]	10 234 [d]	$e_{\pi c}(H_2O)$ 0	ζ 190
	233	16 447 [$^3T_{2g}$] ⟨σ⟩	17 038 [^3E_g] [a]		e_σ(Cl) 6000	
	260	16 502 [$^3T_{2g}$] ⟨π⟩	18 237 [$^3B_{2g}$] [a]		e_π(Cl) 1000	
	282	19 268 [$^3T_{2g}$] ⟨σ⟩				
	507	23 256 [$^3T_{1g}$ (^3P)]	24 360 [^3E_g] [a]			
			28 204 [$^3A_{2g}$] [a]			
		33 092 [{$^3B_{1g}$} $^3A_{2g}$]	34 637 [$^3B_{1g}$] [a]			

Table 2 (*Continued*)

	Raman frequencies 83 K (cm^{-1})	Absorption 5 K (cm^{-1}) [{D_{4h}} O_h (ion)] ⟨polarization⟩	Calculated ligand-field energies [D_{4h} (spin–orbit)]	Emission 5 K (cm^{-1}) [D_{4h}]	Angular overlap parameters for ligand field calculations (cm^{-1})	
$CoCl_2(H_2O)_4 \cdot 2H_2O$	150		167 [(Γ_7) $^4A_{2g}$] [b]		$e_\sigma(H_2O)$ 4300	B 824
	163		919 [^4E_g] [a]		$e_{\pi s}(H_2O)$ 1000	C 3626
	183	8060 [{^4E_g} $^4T_{2g}$]	8054 [$^4B_{2g}$] [a]		$e_{\pi c}(H_2O)$ 400	ζ 516
	199	8330 [{$^4B_{2g}$} $^4T_{2g}$]	8297 [^4E_g] [a]		e_σ(Cl) 3300	
	282	16 450 [{$^4B_{1g}$} $^4A_{2g}$]	16 954 [$^4B_{1g}$] [a]		e_π(Cl) 1000	
	362	18 600 [{^4E_g} $^4T_{1g}$]	18 805 [^4E_g] [a]			
	543	20 268 [{^2E_g} $^2T_{1g}$]	20 273 [(Γ_7)] [b]			
	697	22 250 [{$^4A_{2g}$} $^4T_{1g}$] ⟨π⟩	21 167 [$^4A_{2g}$] [a]			
	851					

[a] Calculated with parameters in the table, $\zeta = 0$.
[b] Calculated with parameters in the table, $\zeta \neq 0$.
[c] Electronic origin of the $^4T_{2g}$ state.
[d] $V(D_2O)_6^{3+}$ in $CsAl(SO_4)_2 \cdot 12D_2O$.

Table 3
Selection rules for electronic transitions in D_{4h} symmetry

Electronic transition	Electric dipole allowed with Γ_u vibration in π polarisation $\langle\Gamma_i\|A_{2u}\|\Gamma_f\rangle = A_{1g}$	Electric dipole allowed with Γ_u vibration in σ polarisation $\langle\Gamma_i\|E_u\|\Gamma_f\rangle = A_{1g}$
$B_{1g} \rightarrow E_g$ or $E_g \rightarrow B_{1g}$	e_u	a_{1u}, a_{2u}, b_{1u}, b_{2u}
$B_{1g} \rightarrow A_{2g}$ or $A_{2g} \rightarrow B_{1g}$	b_{1u}	e_u
$B_{1g} \rightarrow B_{2g}$ or $B_{2g} \rightarrow B_{1g}$	a_{1u}	e_u
$A_{2g} \rightarrow E_g$ or $E_g \rightarrow A_{2g}$	e_u	a_{1u}, a_{2u}, b_{1u}, b_{2u}
$A_{2g} \rightarrow B_{2g}$ or $B_{2g} \rightarrow A_{2g}$	b_{2u}	e_u
$A_{2g} \rightarrow A_{2g}$	a_{2u}	e_u

nickel(II) and cobalt(II) complexes, where the position of hydrogen atoms has been deduced from X-ray crystallographic data [17,18,32]. The angle ψ between the plane of the H_2O ligands with the Cl–M–Cl axis is small, but not exactly zero. Our use of a fixed value of 0 for ψ could be an important reason for the variation of $e_{\pi c}(H_2O)$ between 0 and 700 cm^{-1}. The Racah parameter B was set to 950 cm^{-1} (88% of the free ion value), the ratio C/B to 4 and the spin–orbit coupling constant ζ to 596 cm^{-1}. This AOM calculation does not involve a fit, but it leads to band maxima for $NiCl_2(H_2O)_4$ in satisfactory agreement with the experimental values obtained at 5 K, as shown in Fig. 1 and Table 2.

The calculated energetic order of the excited states in the $^3T_{1g}/^1E_g$ region (O_h) in the D_{4h} point group predicts that the barycenter of the $^3A_{2g}$ state should be lower in energy by 218 cm^{-1} than the barycenter of the ^3E_g state. The $^1A_{1g}$ state is calculated at an energy lower by 55 cm^{-1} than the $^1B_{1g}$ state. This value compares favorably to the average separation of 75 cm^{-1} between the two progressions in the π-polarized absorption spectrum in Fig. 2, especially since no angular overlap parameters were fitted to the spectrum of $NiCl_2(H_2O)_4$.

The experimental spectrum of the *trans*-$NiCl_2(H_2O)_4$ chromophore shows a double progression in π polarization, but only the lower energy progression appears in σ polarization. The maximum of the broad band in σ polarization is at lower energy than in π polarization. The selection rules in the D_{4h} point group are given in Table 3. Transition energies and vibronic patterns can be combined with the calculated crystal field energies, indicating that the $^3B_{1g} \rightarrow {}^3A_{2g}$ band dominates the σ-polarized spectrum. This triplet excited state can only interact with the $^1A_{1g}$ state as established before. The $^3B_{1g} \rightarrow {}^3E_g$ transition is expected at higher energy, as observed in π polarization. The ^3E_g state has A_{1g} and B_{1g} spin–orbit levels that can interact with both singlet excited states, giving rise to a double progression in the spectrum and confirming the energetic order derived from AOM. It is clear from these observations that singlet states gain most of their intensities from the allowed triplet transitions and that intersystem crossings between excited states of different multiplicities can give rise to important vibronic features in the spectra of transition metal complexes.

The absorption band shape for the $^3B_{1g} \rightarrow {}^3A_{2g}/{}^1A_{1g}$ transition has been calculated using the time dependent theory of spectroscopy [14,33–36] and the result is compared to the experimental spectrum in Fig. 4. Spectra of both A_{1g} and E_g spin–orbit levels of the $^3A_{2g}$ and $^1A_{1g}$ states are plotted in the figure. The intensity ratio E_g/A_{1g} is 2:1, based on the degeneracies of the levels, and we assume that the intensity for the transition to the $^1A_{1g}$ state arises entirely from coupling to the triplet state. A simple harmonic surface is used for the E_g level of the $^3A_{2g}$ state, leading to a Poisson band shape. The coupled A_{1g} levels are represented schematically by the potential curves of Fig. 5, the non-harmonic dotted curves clearly show the avoided crossing between the two A_{1g} levels. The relationship between electronic energies for a 'frozen' complex from the AOM calculation and the potential energy surfaces, which correctly characterize the observed absorption spectrum, is illustrated in Fig. 5. The calculated AOM energies define the potential energy surfaces in the Franck–Condon region as indicated in Fig. 5. $NiCl_2(H_2O)_4 \cdot 2H_2O$ provides a clear example of an intersystem crossing where two excited states interact and where the influence from other electronic states is negligible. The one-dimensional potential curves in Fig. 5 quantitatively rationalize all important aspects of the experimental spectrum: the unusually high spacing of the intense vibronic progression and the low-intensity 'interference dip' before the onset of the intense progres-

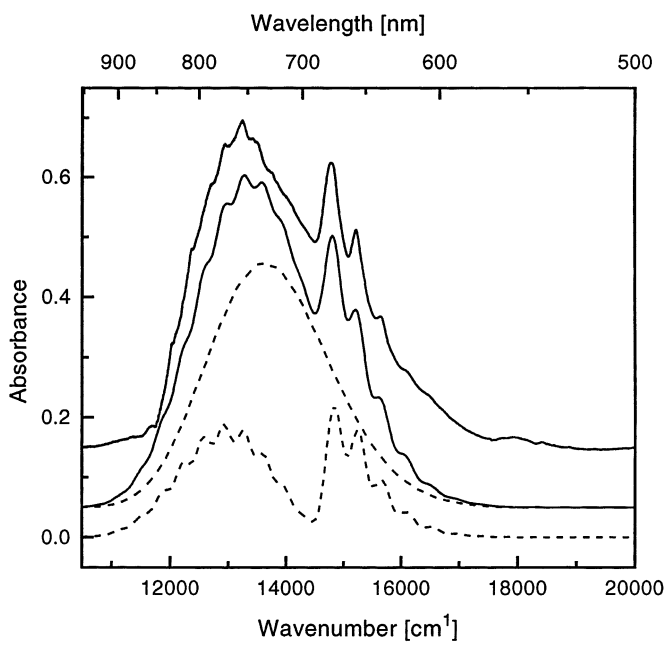

Fig. 4. Calculated and experimental absorption spectra for *trans*-$NiCl_2(H_2O)_4 \cdot 2H_2O$ in σ polarization. The top trace denotes the experimental spectrum, followed by the total calculated spectrum (solid line) separated from the experimental spectrum by 0.1 in absorbance units for clarity. The two dotted traces denote the calculated spectra for the E_g and the coupled A_{1g} levels arising from $^3A_{2g}$ and $^1A_{1g}$.

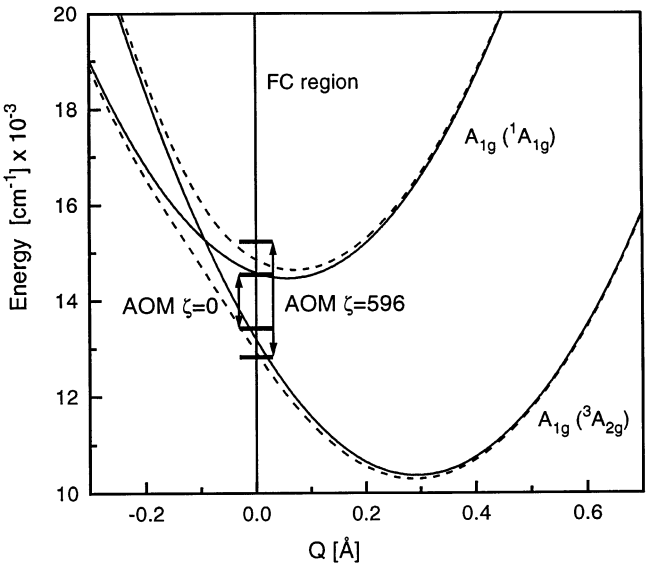

Fig. 5. Potential energy surfaces for the coupled A_{1g} states of $NiCl_2(H_2O)_4{\cdot}2H_2O$. Diabatic and adiabatic potentials are shown as solid and dotted lines, respectively. The horizontal lines separated by arrows in the Frank–Condon region denote the energies of the A_{1g} states calculated with the AOM. The small arrow represents the energy separation without spin–orbit coupling, the tall arrow represents the energy separation with spin–orbit coupling.

sion. It has been shown that this model describes a molecular Fano antiresonance, and an analytical equation for unresolved spectra equivalent to Fig. 4 has been published [37].

4. *trans*-$VCl_2(H_2O)_4^+$

4.1. $Cs_3VCl_6{\cdot}4H_2O$

Recently several ligand field studies were reported for the $[V(H_2O)_6]^{3+}$ cation [30,38–40]. Using AOM, it appears that the anisotropy of the π bonding of the water molecules explains the trigonal splitting observed in the experimental absorption spectra of vanadium(III) hexahydrate [30]. Analogous effects are important in chromium alums [41]. McCarthy et al. [8] have reported a detailed spectroscopic analysis of the $Cs_3VCl_6(X_2O)_4$ compound containing the tetragonal chromophore $VCl_2(X_2O)_4^+$ with X = H or D. The most intriguing feature observed in the literature spectra are two intense maxima separated by about 3000 cm^{-1} in the 500–700 nm region, corresponding to the lowest energy spin-allowed crystal field transitions ($^3T_{1g} \rightarrow {}^3T_{2g}$ in O_h symmetry). We compare several quantitative models for this band system.

The lowest energy electronic transition occurs within the t_{2g}^2 strong field configuration between the $^3T_{1g}$ (^3F) ground state and the $^1T_{2g}$, ^1E_g excited states (O_h symmetry). We present the first experimental measurements of these sharp bands for *trans*-$VCl_2(H_2O)_4^+$ and explore the luminescence spectrum of vanadium(III) aquo complexes.

4.2. Spectroscopic results

The vanadium complexes show intense absorption bands in the UV–Vis range. Three spin-allowed transitions are expected which can be attributed as follows: $^3T_{2g}$ (15000–20000 cm^{-1}), $^3T_{1g}$ (23300 cm^{-1}) and $^3A_{2g}$ (33300 cm^{-1}) (O_h labels). Spin-forbidden absorption transitions can be seen in the NIR region (9600–10400 cm^{-1}) and are assigned to the ^1E_g and $^1T_{2g}$ (O_h labels). These NIR spectra show many interesting features and are presented in Fig. 9. At least nine sharp transitions can be identified with widths at half height varying between 6 and 15 cm^{-1}. The overall oscillator strengths f are estimated to be 1.73×10^{-8} and 5.8×10^{-5} for the singlets and the $^3T_{2g}$ transitions, respectively. The first value is typical for spin-forbidden and parity-forbidden transitions, while the second one, with an oscillator strength about three orders of magnitude higher, is in the range expected for the spin-allowed d–d bands.

An attempt to measure polarized absorption spectra for the singlet states (9600–10400 cm^{-1}) did not lead to well-defined dichroic ratios. At the weak absorbance of the singlet states, the background noise of the spectrometer is increased due to the polarizers in this region of low detector sensitivity. With the instrumentation described before we were unable to detect any luminescence from $Cs_3VCl_6{\cdot}4D_2O$. This is due to the low quantum yield of each individual complex and to energy transfer processes in the concentrated solid. We did observe a sharp luminescence transition from $V(D_2O)_6^{3+}$ doped into $CsAl(SO_4)_2{\cdot}12D_2O$ at 10234 cm^{-1} (5 K), in exact agreement with the lowest-energy absorption transition (see Table 2 and Ref. [38]). This comparison shows that the weak intraconfigurational transitions are lower in energy by approximately 520 cm^{-1} for *trans*-$VCl_2(H_2O)_4^+$ than for $V(H_2O)_6^{3+}$ complexes [38], again underlying the very specific electronic structure of the title chromophores.

The 15000–20000 cm^{-1} region contains the most interesting polarization effects. Fig. 6 shows that a single maximum is obtained in π polarization. In σ polarization, two maxima with a separation of about 3000 cm^{-1} are observed. McCarthy et al. [8] have reported the third polarization, in which the spectrum is almost identical to the σ spectrum of Fig. 6. These observations agree with the expected polarization for a Jahn–Teller E_g state in D_{4h} symmetry, as established by Hougen [42].

The Raman spectra at 83 K are shown for both compounds in Fig. 7. Five Raman active modes are expected for a seven-atom D_{4h} complex. It appears that they are all observed between 150 and 550 cm^{-1}. Three of them shift upon deuteration and are denoted by the arrows. The 507 cm^{-1} peak (482 cm^{-1} in the deuterated compound) can be assigned to the totally symmetric ν(V–O) mode. This

frequency is close to the 530 cm^{-1} value recently observed for $V(H_2O)_6^{3+}$ in alums [38]. The other two modes involving the water ligand should be of b_{1g} and b_{2g} symmetry in the D_{4h} point group. Their assignment is doubtful, but the only deuteration sensitive peaks between 150 and 507 cm^{-1} are the 260 and 233 cm^{-1} bands (246 cm^{-1} and 221 cm^{-1} in the deuterated compound). The other two modes which do not significantly depend upon deuteration are assigned as the a_{1g} ν(V–Cl) and the e_g δ(V–Cl) vibrations.

4.3. The double maximum of the lowest energy triplet band: quantitative comparison of models

The absorption spectrum of the $VCl_2(H_2O)_4^+$ cation in $Cs_3VCl_6(H_2O)_4$ in σ polarization shows a splitting of 3000 cm^{-1} for the lowest energy triplet band, suggesting a separation of the first triplet excited state, $^3T_{2g}$ (O_h). The splitting in $Cs_3VCl_6{\cdot}4H_2O$ is too large to be explained by the tetragonal field and all attempts to reproduce it with the angular overlap formalism failed, even when π anisotropy for the water ligand is taken in account. We include energies calculated with the

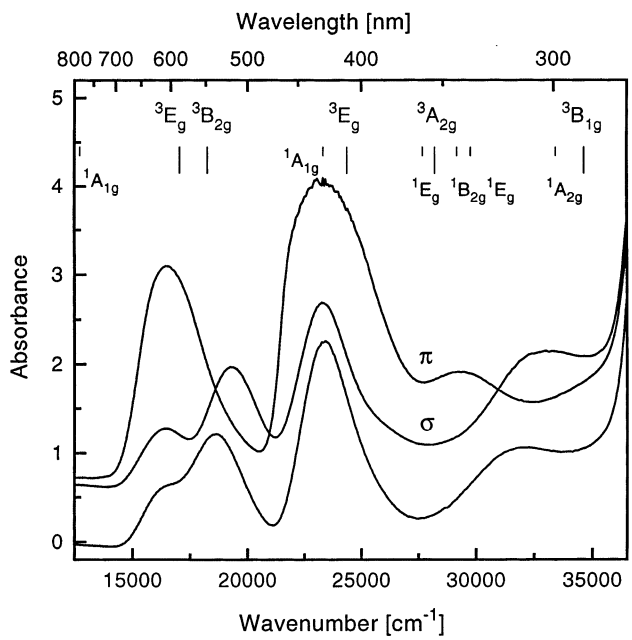

Fig. 6. Polarized absorption spectra of $Cs_3VCl_6(H_2O)_4$ at 80 K (top). The polarization directions are given relative to the Cl–V–Cl axis of the *trans*-$VCl_2(H_2O)_4^+$ chromophore. The bottom trace is the σ polarized spectrum of $Cs_3VCl_6(D_2O)_4$ at 25 K. The π polarized spectrum of the deuterated compound is similar to the undeuterated π spectrum. The vertical lines represent the AOM energies calculated with parameters from Table 2 with $\zeta = 0$. The tall lines represent spin-allowed transitions, the short lines the spin-forbidden transitions.

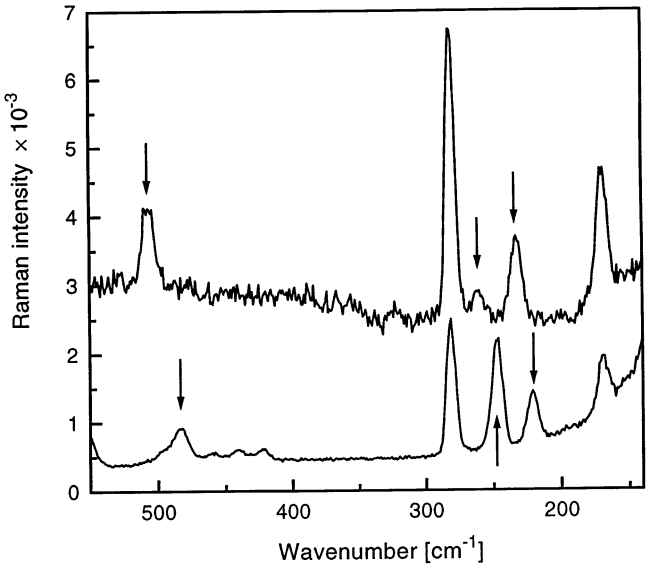

Fig. 7. Unpolarized Raman spectra of $Cs_3VCl_6(H_2O)_4$ (top trace) and $Cs_3VCl_6(D_2O)_4$ (bottom trace) at 77 K. The arrows denote the three vibrational modes involving the water ligands.

AOM model in Table 2 in order to illustrate this discrepancy. The calculated energy difference between the ^3E_g and $^3B_{2g}$ states arising from $^3T_{2g}$ (O_h) in D_{4h} symmetry is 1200 cm^{-1}, corresponding to less than 50% of the experimental energy difference of 2800 cm^{-1} between the two maxima in the sigma polarized spectrum in Fig. 6. McCarthy et al. [8] have suggested that the splitting is due to bands involving vibronic OH modes, but the intensity of the band is quite high in comparison to many other transition metal aquo complexes (see Fig. 16), where only weak transitions involving OH stretching modes are observed [24].

We have shown that spin–orbit coupling between triplet and singlet states of nickel(II) complexes is of importance and is essential to explain many spectroscopic observations [1]. The two maxima observed for the vanadium(III) complex could be attributed to a singlet and a triplet state, in direct analogy with the nickel(II) spectra discussed in the preceding section. A $^1A_{1g}$ state is expected for the $VCl_2(H_2O)_4^+$ cation in the 500 nm region, but there are substantial differences between the vanadium(III) and the nickel(II) complexes. First and most important, the spin–orbit coupling constant (λ) for vanadium(III) is expected to be approximately 95 cm^{-1}, much lower than for the nickel(II) ion. Second, the matrix element between the $^1A_{1g}$ and the $^3T_{2g}$ (O_h) states is zero. In D_{4h} symmetry coupling can occur, but the non-zero matrix elements are smaller by approximately two orders of magnitude than for the nickel(II) complexes discussed in the preceding section. AOM calculations show that there are several matrix elements that play a role — small ones (that are zero in O_h) between energetically close states, and larger ones between states with a large energy separation, as mentioned for $^3T_{1g}$ (O_h). One can

consider coupling with the higher energy $^3T_{1g}$ (O_h) state, but in this case the splitting is approximately 3700 cm^{-1} and the matrix element is $-2\lambda\sqrt{2}$. The splitting should be of the order of two times the absolute value of the matrix element and the intensity of the forbidden band decreases rapidly for larger splitting [43]. We are therefore not able to explain the observation with spin–orbit coupling in a reasonable way. The separation of the singlet and triplet states is too large and the matrix element too small.

A first alternative explanation involves vibronic coupling with OH stretching modes, as suggested by McCarthy et al. [8]. The hypothesis of progressions in OH or OD totally symmetric stretching modes (a_{1g}) was tested with aquo and deuterated compounds. As shown in the top panel of Fig. 8, a calculated spectrum with a progression in the OH stretching a_{1g} mode is in good agreement with the two maxima of the experimental spectrum of $Cs_3VCl_6{\cdot}4H_2O$. The correlation for the OD vibration is not as good as for OH. The parameters used for the simulations are shown in Table 5. Fig. 8 shows that the third member of the progression has no equivalent in the experimental spectra. Only an ungerade parity vibronic origin can

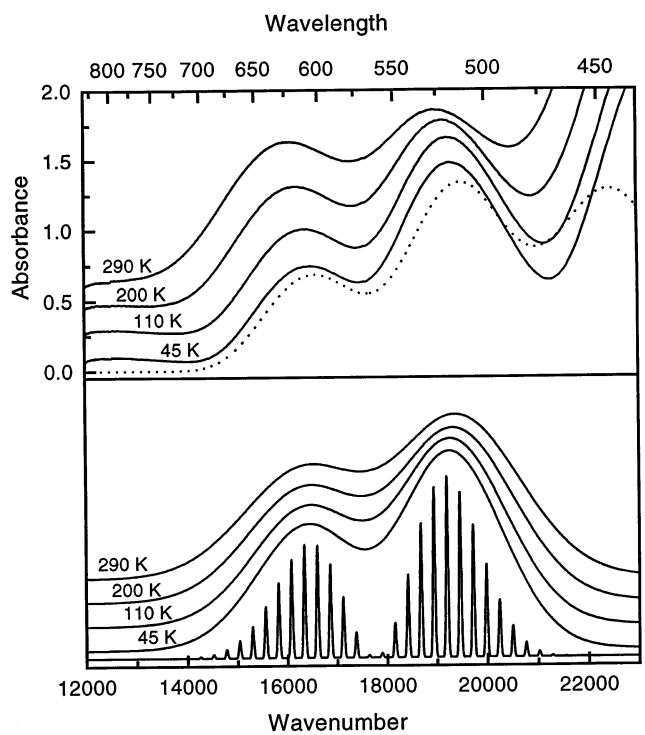

Fig. 8. Temperature dependence of the $^3T_{2g}$ (O_h label) σ polarized absorption spectrum of $Cs_3VCl_6(H_2O)_4$ (top panel). The dotted trace denotes a calculated spectrum involving a progression in the OH totally symmetric stretching mode. The bottom panel shows the calculated temperature dependence, using the Jahn–Teller model described in the text with the calculated resolved vibrational structure shown as the bottom trace.

account for the lack of further vibronic members in the progression. All ungerade parity vibrations, which can lead to electric dipole allowed vibronic origins, are given in Table 3. It is unusual, but not without precedent, that a vibronic origin occurs in a high-frequency mode. A detailed analysis of such a spectrum with resolved vibronic structure was recently given for the organometallic compound $Ta(CO)_6$, where a high-frequency C≡O mode acts as a vibronic origin [44]. This explanation is qualitatively reasonable for $VCl_2(H_2O)_4^+$, and it shows the importance of coordinate dependent transition dipoles. This model can explain why a double maximum is observed for $VCl_2(H_2O)_4^+$, but it cannot account for its absence in the spectrum of $V(H_2O)_6^{3+}$. Vibronic origins involving high-frequency modes of the H_2O ligands of the title complexes are compared in the final section of this article and in Fig. 16.

A second alternative explanation for the observed double maximum involves a Jahn–Teller effect. In the D_{4h} point group, the $^3T_{2g}$ state (O_h) is split by the tetragonal field into a $^3B_{2g}$ and a ^3E_g state. Two maxima can occur due to a Jahn–Teller effect involving the ^3E_g state and the b_{1g} and b_{2g} modes. The observed spectra could be a combination of both a Jahn–Teller effect along metal–ligand modes with a contribution from OH (or OD) vibrational modes, as discussed in the preceding paragraph. In Fig. 8, we present a model calculation involving a Jahn–Teller effect involving the b_{1g} and b_{2g} metal–ligand modes. We use a model based on an $E_g \otimes (b_{1g}, b_{2g})$ Jahn–Teller effect [42,45]. In our approach, we neglect spin–orbit coupling, which is quite small for V^{3+} compounds. Ballhausen [45] has shown that for low spin–orbit coupling ($\lambda \approx 100\ cm^{-1}$) in tetragonal molecules, the overall band shape of the E_g state is not changed by spin–orbit coupling, but only the resolved fine structure is affected. Since no resolved vibronic structure is observed for this compound in the region of the $^3B_{2g}$ and ^3E_g transitions, we neglect spin–orbit coupling to simplify the problem. The experimental temperature dependence of the σ polarized absorption spectrum is shown in the top panel of Fig. 8 and compared to the calculated temperature dependence using the model described here in the bottom panel of Fig. 8.

In an octahedrally coordinated compound, it is tempting to assume that a $T \otimes e_g$ Jahn–Teller effect can be responsible for such a splitting. For low spin–orbit coupling, when only a twofold degenerate e_g vibration is involved, this is impossible due to the orthogonality of the three T electronic states [46,47]. In contrast, it is known that an $A \rightarrow E$ electronic transition can give rise to a large splitting of the absorption band [46,48]. This shows that the tetragonal symmetry of the molecule plays a crucial role in the observation of the double maximum. It could also explain the absence of a double maximum for the corresponding band in $V(H_2O)_6^{3+}$.

We use two Jahn–Teller active vibrational frequencies ω_1 and ω_2 of b_{1g} and b_{2g} symmetry with Jahn–Teller couplings of f_1 and f_2, respectively. We can describe three limiting cases [42]: (1) f_1 or $f_2 = 0$, a case where only one vibrational frequency remains and the E_g level is split into two orthogonal electronic states. The vibrational levels of the two electronic states are degenerate, a situation known as accidental Born–Oppenheimer degeneracy [42]. (2) If $f_1 = f_2$ and $\omega_1 = \omega_2$ the problem is identical to an $E_g \otimes e_g$ Jahn–Teller problem in octahedral symmetry. In

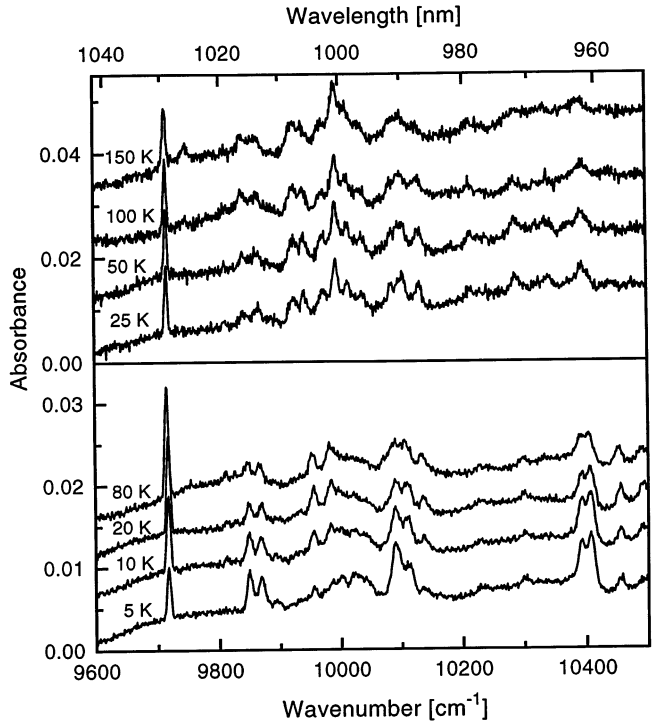

Fig. 9. Temperature dependence of the unpolarized absorption spectra in the region of ^1E_g and $^1T_{2g}$ (O_h labels) spin-flip transitions of $Cs_3VCl_6(D_2O)_4$ (top panel) and $Cs_3VCl_6(H_2O)_4$ (bottom panel).

this case, the potential surface has cylindrical symmetry and this problem has been solved by Longuet-Higgins et al. [48]. (3) For arbitrary values of ω_1, ω_2, f_1 and f_2, the problem is more difficult to solve. In that case, the potential surface has twofold symmetry about the energy axis [46]. If by chance $\omega_1 = \omega_2$, the potential surface happens to have cylindrical symmetry [46].

We make the following approximations: (1) ω_1 and ω_2 are sufficiently close to assume cylindrical symmetry of the potential surface. The vibronic intervals of 260 and 233 cm^{-1} in Fig. 9 confirm this assumption. (2) f_1 and f_2 are sufficiently close to allow rotation of the molecule between an elongated and a rhombic configuration [45]. If these conditions are respected, then the problem is reduced to an $E_g \otimes e_g$ Jahn–Teller interaction.

We use a one-dimensional model in which the potential surface is a slice through the more complex two-dimensional cylindrical $E_g \otimes e_g$ potential surface. In that approximation, the vibrational wavefunctions of the degenerate E_g state are harmonic and degenerate. The probability distribution of the first vibrational wave function of the non-degenerate A electronic ground state in the cylindrical potential is $2\alpha^2\rho\ e^{-\alpha^2\rho^2}$. The parameter α is defined as $(K\mu/\hbar^2)^{1/4}$ and ρ denotes the radius in the cylindrical coordinate system. We apply the simple model developed by

Longuet-Higgins et al. [48] in which the E state is split by a linear coupling constant of the form $\kappa\rho$. In this model $\kappa^2 = 2\Delta E/\hbar\omega$ and the parameters used for the simulation are shown in Table 5. The potential energy surfaces for the E_g states are represented by the matrix:

$$V_{E_g} = \begin{pmatrix} \frac{K\rho^2}{2} & \kappa\rho \\ \kappa\rho & \frac{K\rho^2}{2} \end{pmatrix} \quad (1)$$

The experimental band with its double maximum can not be rationalized with purely electronic models, such as AOM calculations. Vibronic effects have the most important influence on the spectrum. The change of the energy difference between the maxima with deuteration is evidence for vibronic origins involving OH and OD modes, and the observation of the double maximum only in D_{4h} symmetry is a signature of a possible Jahn–Teller effect involving only the ^3E_g state. It is likely that a combination of these two vibronic effects occurs, but the unresolved experimental spectrum does not allow us determine their individual contributions.

4.4. Ground state splitting and spin–orbit interaction between the lowest energy singlet and triplet states

AOM calculations were also made in order to verify that the band positions could be reproduced without major discrepancies (except for the splitting of the lowest energy triplet band). Using the zero field splitting of $Cs_3VCl_6{\cdot}4H_2O$ reported by Carlin et al. [49], we set $^3A_{2g}$ (D_{4h}) as the ground state with a splitting of 8 cm^{-1}. The second component of the $^3T_{1g}$ (O_h) ground state, the ^3E_g (D_{4h}) level, is expected to be around 1000 cm^{-1} [49]. We use AOM with spin–orbit coupling to exactly reproduce the 8 cm^{-1} splitting of the ground state. The spin–orbit coupling constant ζ was set to 190 cm^{-1} ($\lambda = 95$ cm^{-1}) for all calculations, see Tables 1 and 4. Table 2 and Fig. 6 show that the positions of the bands are reasonably reproduced.

The well-resolved NIR absorption transitions allow us to derive quantitative information on singlet–triplet interactions and the splitting of the electronic ground state. The temperature dependence of the lowest energy singlet absorption for $Cs_3VCl_6{\cdot}4H_2O$ and for $Cs_3VCl_6{\cdot}4D_2O$ is plotted in Fig. 9. The bottom panel shows that the intensity of the transition decreases from 80 to 5 K. We use Boltzmann statistics (Eq. (2)) to fit this temperature dependence assuming a 8 cm^{-1} splitting d of the ground state [49].

$$I(T) = \frac{2E\, e^{-(d/0.693816T)}}{1 + 2\, e^{-(d/0.693816T)}} + \frac{A}{1 + 2\, e^{(-d/0.693816T)}} \quad (2)$$

The result of this calculation is shown in Fig. 10. The best agreement with the experimental data is obtained with a higher value for E than for A, where A and E denote the intensities from the A_{1g} and E_g levels, respectively. The E_g sublevel is

located 8 cm^{-1} above the A_{1g} sublevel and the intensity gain arises from thermal population of this E_g level.

Spin–orbit effects are quite weak in vanadium(III) complexes, as indicated by the low intensity of the singlet transitions in comparison to the triplet bands. We report a spin–orbit calculation for the first singlet and triplet bands in the absorption spectrum of $Cs_3VCl_6{\cdot}4H_2O$ in Fig. 10. The calculated ratio $I_{triplet}/I_{singlet}$ is near the experimental ratio of 1118, a much higher value than for the nickel(II) and chromium(III) complexes. The singlet and triplet bands are well separated in the vanadium(III) complexes and the experimental ratio of intensities can be accurately calculated. We include both maxima observed between 14000 and 22000 cm^{-1} to calculate the intensity of the spin-allowed band. If only the first or only the second band is integrated to calculate the intensity, the experimental ratio is 2.5 times higher than the calculated one. All the models discussed for this band indicate that both maxima are part of the triplet transition and we obtain a calculated $I_{triplet}/I_{singlet}$ ratio of 1275, slightly higher than the experimental value of 1118, as shown in Table 1. This excellent agreement again indicates that the double maximum discussed in the preceding section corresponds to a transition to a single excited electronic state, and not to the two states arising from $^3T_{2g}$ (O_h) in D_{4h} symmetry, illustrating again that the bandshape of the first spin allowed band in *trans*-$VCl_2(H_2O)_4^+$ is defined by vibronic effects (Table 5).

Table 4
Spectroscopic parameters for coupled electronic states

Parameters (O_h labels)	$^1T_{2g}$–$^3T_{2g}$ $Cs_3VCl_6{\cdot}4H_2O$	$^1A_{1g}$–$^3T_{1g}$ $Cs_3VCl_6{\cdot}4H_2O$	$^3T_{1g}$–^1E_g $NiCl_2(H_2O)_4{\cdot}2H_2O$	$^4T_{2g}$–^2E_g $Cs_2CrCl_5{\cdot}4H_2O$
Allowed transition origin(s) (cm^{-1})	14 386 (all $^3T_{2g}$ s.o. sub-levels)	21 000 (all $^3T_{1g}$ s.o. sub-levels)	10 365 A_{1g} ($^3A_{2g}$) 10 500 E_g ($^3A_{2g}$)	13 722.5 U (^4E_g, $^4T_{2g}$) 13 655.4 ($^4B_{2g}$, $^4T_{2g}$)
Forbidden transition origin (cm^{-1})	9717 T_{2g} ($^1T_{2g}$) (O_h label)	19 000 A_{1g} ($^1A_{1g}$) (O_h label)	14 403 A_{1g} ($^1A_{1g}$)	14 437.9 U (^2E_g)
Vibrational frequencies (cm^{-1})				
$\hbar\omega$ g.s.	507	507	364	286
$\hbar\omega$ allowed e.s.	507	507	357	286
$\hbar\omega$ forbidden e.s.	507	507	364	286
ΔQ_T, allowed (Å)	0.18	0.18	0.295	0.265
ΔQ_S, forbidden (Å)	0.0	0.0	0.05	0.0
Matrix element V_{ST} (cm^{-1})	-232.7 ($-\lambda\sqrt{6}$)	-268.7 ($-2\lambda\sqrt{2}$)	730 ($-\lambda\sqrt{6}$)	-187 ($-3\lambda\sqrt{6}/\sqrt{5}$)
Coupling constant λ (cm^{-1})	95	95	-270	57
Damping factor Γ (cm^{-1})	250 ($^3\Gamma$), 10($^1\Gamma$)	250	100	200 ($^4\Gamma$), 10($^2\Gamma$)
Transition dipole moments $\mu_{forbidden}/\mu_{allowed}$	0.00/1.00	0.00/1.00	0.09/0.91	0.00/1.00

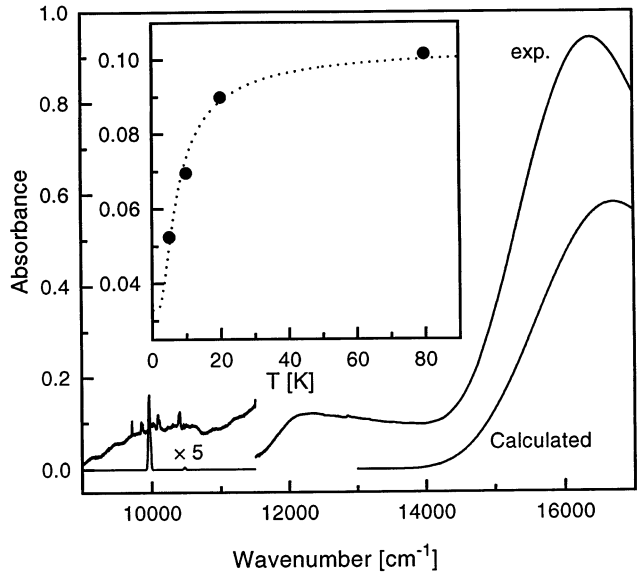

Fig. 10. Calculation of the lowest $^1T_{2g}$ and $^3T_{2g}$ (O_h labels) bands in $Cs_3VCl_6{\cdot}4H_2O$. The calculated triplet intensity is normalized to the unpolarized $^3T_{2g}$ band in the 15000 to 20000 cm^{-1} region. The dots show the temperature dependence of the intensity of the first NIR absorption peak centered at 9717 cm^{-1} for $Cs_3VCl_6(H_2O)_4$. The dashed line is obtained from the fit of Eq. (2) to the experiment, with a zero field splitting of 8 cm^{-1}.

Table 5
Spectroscopic parameters for the $^3T_{2g}$ (O_h) state in $Cs_3VCl_6{\cdot}4H_2O$

Parameters	Jahn–Teller ^3E_g	OH vibration		
$^3\Gamma$ origin (cm^{-1})	11 000	12 380		
Vibrational frequencies (cm^{-1})	260	3000	507 ν(VO)	282 ν(VCl)
Distortion, ΔQ (Å)		0.196	0.152	0.145
κ^2 [48]	50			
Damping factor Γ (cm^{-1})	550–700	100		

5. *trans*-$CrCl_2(H_2O)_4^+$

5.1. $Cs_2CrCl_5{\cdot}4H_2O$

Crystallographic studies reveal that the green $CrCl_3{\cdot}6H_2O$ and $Cs_2CrCl_5(H_2O)_4$ crystals contain the *trans*-$CrCl_2(H_2O)_4^+$ chromophore [21–23]. $Cs_2CrCl_5(H_2O)_4$ is more suitable for spectroscopic investigations because it is more stable and its crystals are of higher optical quality than those of $CrCl_3{\cdot}6H_2O$ [7]. The intensity of the first spin forbidden transition in this *trans*-dichlorotetraaquo chromophore is intermediate between those for the nickel(II) and vanadium(III) analogs. The

separation between this transition and the first allowed band is also intermediate, as expected from their intensities. In a simple perturbation treatment, the intensity of the forbidden transition varies proportionally to $\zeta^2/\Delta E^2$ [43], where ΔE is the separation of the doublet and the closest quartet states and ζ is the spin–orbit coupling constant. The chromium(III) complex clearly illustrates the intermediate case between strong (nickel) and weak (vanadium) coupling.

5.2. Spectroscopic results

The low-temperature single crystal absorption spectra of $Cs_2CrCl_5{\cdot}4X_2O$ are shown in Fig. 11. The spectra of this dicesium compound are identical to those reported previously by McCarthy et al. [7]. Only the first quartet states which all arise from the ^4F free ion term can be clearly seen in the absorption spectra shown in Fig. 11. The transitions to the ^2E_g and $^2T_{1g}$ (O_h) doublet states are reported in detail in Fig. 12. The origin of the first doublet band is at 14438 cm^{-1}, expected to be a component of ^2E_g (O_h) split by the tetragonal field. The exact position of the $^2T_{1g}$ state is not easily assigned within the sharp peaks between 14500 and 16000 cm^{-1} [7]. A higher $^2T_{2g}$ state (O_h) is seen around 22000 cm^{-1}, but the exact

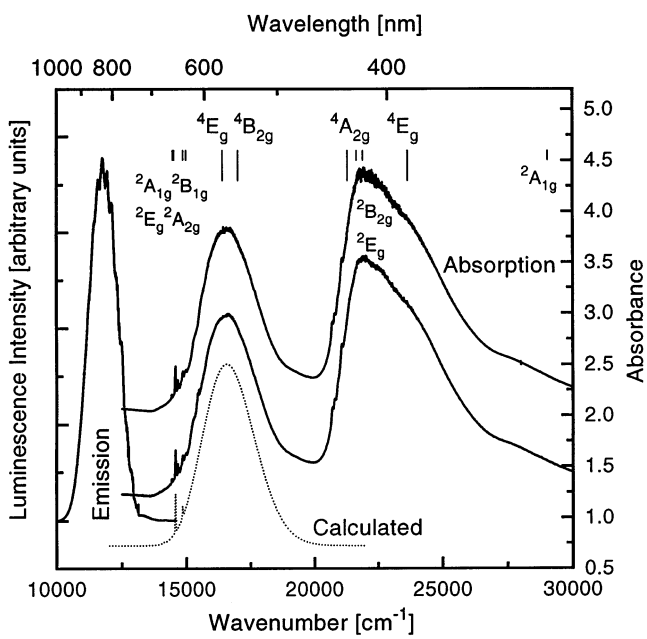

Fig. 11. Unpolarized absorption spectra of $Cs_2CrCl_5{\cdot}4H_2O$ (bottom trace) and $Cs_2CrCl_5{\cdot}4D_2O$ (top trace) at 5 K. The trace at lower energy than the absorption spectra is the emission spectrum of $Cs_2CrCl_5{\cdot}4H_2O$ at 5 K. The dotted trace denotes the calculated spectrum for the first quartet and doublet states. The vertical lines represent the AOM energies calculated with parameters from Table 2 with $\zeta = 0$. The tall lines represent spin-allowed transitions, the short lines the spin-forbidden transitions.

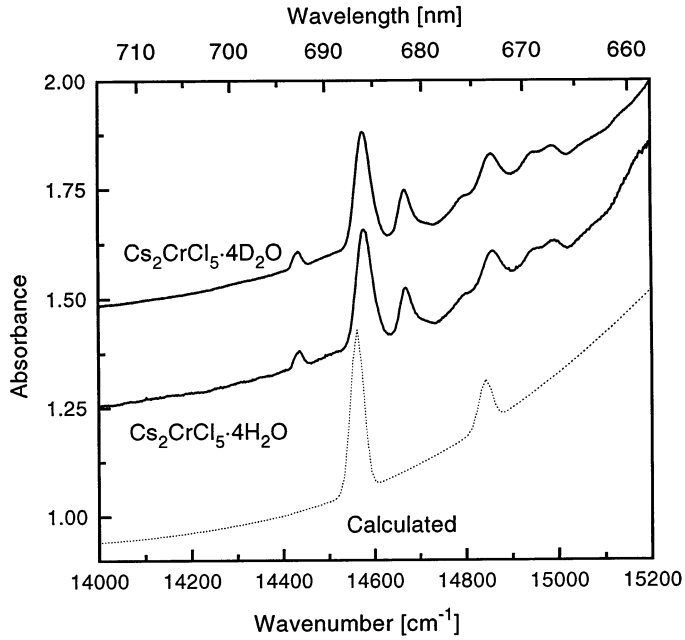

Fig. 12. First transitions to ^2E_g and $^2T_{1g}$ (O_h notation) in $Cs_2CrCl_5{\cdot}4H_2O$ (bottom trace) and $Cs_2CrCl_5{\cdot}4D_2O$ (top trace). The dotted trace denotes the calculated spectrum.

position of its electronic origin cannot be precisely determined due to overlap with more intense allowed transitions.

We compare the observed transition energies in Fig. 11 to AOM calculations. The angular overlap parameters $e_\sigma(H_2O)$, $e_{\pi s}(H_2O)$ and $e_{\pi c}(H_2O)$ for the chromium(III) complex are 7000, 1000 and 500 cm^{-1}, respectively. For $e_\sigma(Cl)$ and $e_\pi(Cl)$, values of 6000 and 1000 cm^{-1} were used. The ligand-field parameters B and C and the energies in Table 2 are in reasonable agreement with the values reported by McCarthy et al. [7], and the overall agreement between calculated and observed transitions is good, as illustrated in Fig. 11. A recent paper on the energy levels of tetragonal chromium(III) complexes in solution [50] reports calculated energies that are not significantly different from ours.

There are numerous emission spectra of hexaaquochromium(III) reported in the literature [41,51–53]. Chromium(III) halide complexes have also been studied by luminescence spectroscopy [54,55], but only a few luminescence spectra of tetragonal chromium complexes are reported [56]. To our knowledge, no luminescence spectra of dichlorotetraaquochromium(III) have been published. The emission spectrum of $Cs_2CrCl_5{\cdot}4H_2O$ is shown in Figs. 11 and 13. At 5 K, a large emission band from $^4T_{2g}$ (O_h) can be observed as shown in Fig. 11 and its electronic origin is clearly detected at 13655 cm^{-1}, as indicated by the arrow in Fig. 13. The broad band indicates that emission occurs from the lowest energy quartet state. High-temperature fluorescence for chromium(III) aquo complexes has been reported by Forster [52], but to our knowledge Figs. 11 and 13 present the first quartet–quartet

emission with resolved vibronic structure observed at low temperature for a chromium(III) complex with aquo ligands.

We have also measured the luminescence spectra of the *trans*-dichlorotetraaquochromium chromophore in green $CrCl_3 \cdot 6H_2O$ and in green $Cr:AlCl_3 \cdot 6H_2O$, illustrated in Fig. 14. Both spectra are similar. The high-energy region in the spectrum of $Cr:AlCl_3 \cdot 6H_2O$ is probably due to luminescence from $Cr(H_2O)_6^{3+}$. It is well known that different chloroaquochromium(III) isomers are formed in solution [23]. $Cr(H_2O)_6^{3+}$ doped into $AlCl_3 \cdot 6H_2O$ leads to sky-blue crystals [52], while $CrCl_2(H_2O)_4^{+}$ and $CrCl(H_2O)_5^{2+}$ lead to green crystals. The luminescence spectra in Fig. 14 consist of a series of sharp bands arising all from the ^2E_g (O_h) state. In $Cs_2CrCl_5 \cdot 4H_2O$, the electronic origin of the quartet state is at lower energy than the origin of the emitting doublet states in Fig. 14. This is the main spectroscopic difference between this solid and the green $CrCl_3 \cdot 6H_2O$, which contains luminophores with a very similar ligand sphere. The two chloride ligands of *trans*-dichlorotetraaquo-chromium(III) appear to be sufficient to lead to a quartet emitting state, as observed for the limiting situation of a ligand environment consisting entirely of chloride ligands in $CrCl_6^{3-}$ [55]. Other factors favoring luminescence from a quartet state include a strong splitting of the $^4T_{2g}$ (O_h) state lowering the electronic origin of a quartet component below the origin of the ^2E_g (O_h) state. The Jahn–Teller splitting of the ^4E_g state (D_{4h}) could also lead to a particularly low-energy quartet component. The $t_{2g}^2 e_g^1$ electronic configuration of the

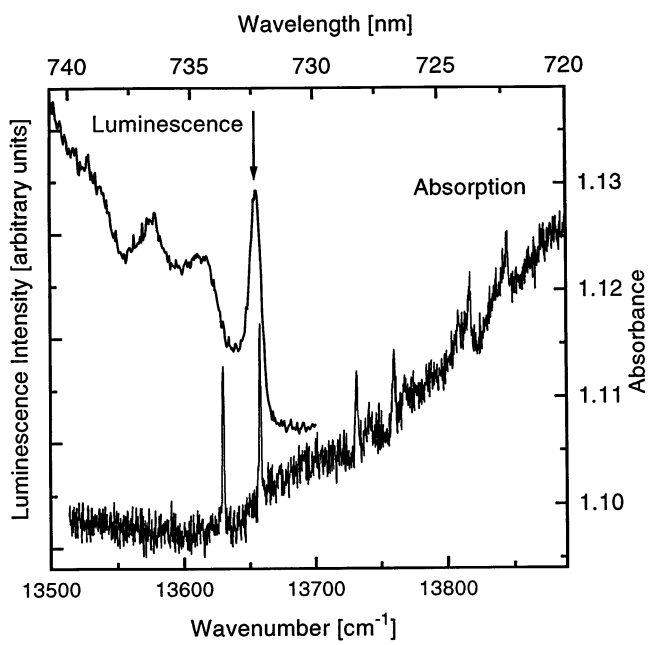

Fig. 13. Unpolarized absorption spectrum of $Cs_2CrCl_5 \cdot 4H_2O$ (bottom trace) and emission spectrum (top trace) at 5 K. The arrow denotes the origin of the emission spectrum at 5 K.

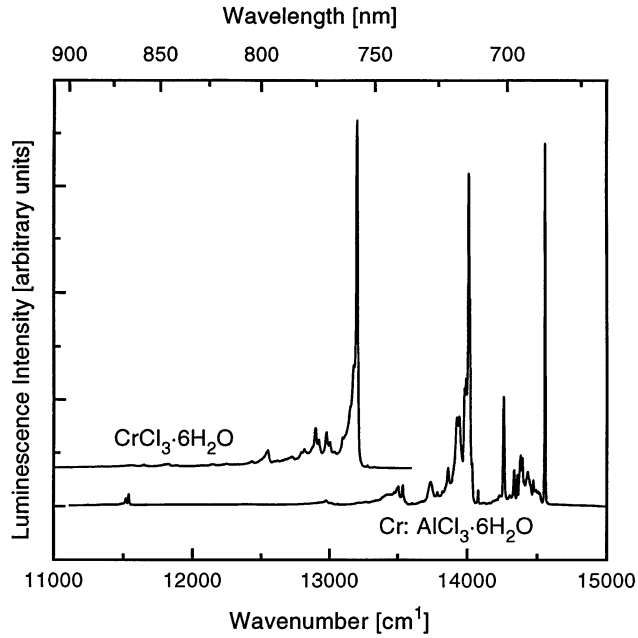

Fig. 14. Emission spectra of green $CrCl_3{\cdot}6H_2O$ (top trace) and green $Cr{:}AlCl_3{\cdot}6H_2O$ (bottom trace) at 5 K. Both samples contain the $CrCl_2(H_2O)_4^+$ chromophore, but $AlCl_3{\cdot}6H_2O$ can also contain the $Cr(H_2O)_6^{3+}$ and $CrCl(H_2O)_5^{2+}$ chromophores.

^4E_g state is susceptible to a strong Jahn–Teller effect, and the main progression observed in the luminescence spectrum (see Fig. 11) has an energy interval of 200 cm^{-1}, significantly different from the totally symmetric ν(Cr–Cl) and ν(Cr–O) modes observed in the Raman spectrum (286 and 484 cm^{-1}, respectively, see Table 2). This is evidence for distortions involving non-totally symmetric modes in the quartet excited state. All these effects are likely to play an important role in the luminescence behavior of $Cs_2CrCl_5{\cdot}4H_2O$.

The photophysics and photochemistry of aquo-chromium(III) complexes has been extensively studied in the past by several authors [52,57–60]. We report new lifetime measurements on $CrCl_3{\cdot}6H_2O$, $Cr(H_2O)_6^{3+}$ (in $AlCl_3{\cdot}6H_2O$) and $Cr(D_2O)_6^{3+}$ (in $ND_4Al(SO_4)_2{\cdot}12D_2O$). For $Cr(D_2O)_6^{3+}$ we obtained a value for $(\tau p^0)^{-1}$ of 2805 s^{-1} ($\tau = 357$ μs at 5 K) which is very close to the value of 2860 s^{-1} ($\tau = 350$ μs) obtained by Camassei and Forster [52] for $Cr(D_2O)_6^{3+}$ in $AlCl_3{\cdot}6D_2O$. We have measured the values of $(\tau p^0)^{-1}$ for $Cr(H_2O)_6^{3+}$ and $CrCl_2(H_2O)_4^+$ (in green $CrCl_3{\cdot}6H_2O$) of 105165 ($\tau = 9.5$ μs) and 47740 s^{-1} ($\tau = 21$ μs), respectively, at 5 K. The lifetime of the *trans*-dichloro compound is more than twice the lifetime of the hexaaquo complex, a difference possibly due to the lower number of OH oscillators in the $CrCl_2(H_2O)_4^+$ chromophore. This comparison shows that lifetimes are very dependent on the number of water molecules coordinated to the chromium-(III) cation, indicating that the main relaxation process is non-radiative. $Cr(D_2O)^{3+}$

and $Cr(H_2O)^{3+}$ are both emitting from ^2E_g state, but the deuterated compound has a lifetime that is more than 30 times longer. This comparison indicates that lifetime measurements on these compounds cannot give reliable information on the spin multiplicity and other characteristics of the emitting state, since the non-radiative decay is always faster by several orders of magnitude than radiative processes.

The Raman spectrum of $Cs_2CrCl_3(H_2O)_4$ at 83 K is very similar to the spectrum of the analogous vanadium compound showing the five Raman active modes expected for a seven-atom D_{4h} complex. Their vibrational frequencies are observed between 150 and 550 cm^{-1} and they differ by only a few wavenumbers from those of the vanadium complexes. A recent publication reports the infrared and Raman spectroscopy of the green pseudotetragonal form of $CrCl_3 \cdot 6H_2O$ and its deuterated analog at room temperature [61] and two strong bands at 463 cm^{-1} ν(Cr–O) and 295 cm^{-1} ν(Cr–Cl) were observed, frequencies that compare well with our results in Table 2.

5.3. Intersystem crossing and vibronic structure: intermediate effects caused by spin–orbit coupling

The intensity of the first forbidden transition in the aquo-chloro complexes of chromium(III) is intermediate between those of the vanadium(III) and nickel(II) analogs. The first singlet band of the $VCl_2(H_2O)_4^+$ chromophore is very weak and hard to detect in absorption experiments. The first forbidden doublet of the $CrCl_2(H_2O)_4^+$ chromophore is easily seen, but its intensity is much lower than that of the first spin-forbidden band of $NiCl_2(H_2O)_4$ (see Table 1).

There are two doublet states around 700 nm (14300 cm^{-1}) for the chromium compound, ^2E_g and $^2T_{1g}$ (O_h). Spin–orbit coupling transforms the ^2E_g to U and the $^2T_{2g}$ to E′ and U. These levels can all interact with the $^4T_{2g}$ state which is split into E′, E″ and 2U. Only the twofold degenerate E″ component of the quadruplet remains uncoupled to the doublet states in O_h symmetry [5]. There is no U state in D_{4h} symmetry, all levels are of E′ or E″ symmetry. This peculiarity of the D_{4h} point group leads to very complicated interactions due to a large number of states of identical symmetry that can couple together and for that reason we treat the problem in approximate O_h symmetry. The model presented in the following is based on two coupled electronic states whose potential energy surfaces are defined along a single normal coordinate. It is therefore a semi-quantitative model, able to reproduce the intensity ratio between the allowed and forbidden bands, but not the resolved structure observed in Fig. 12. We have recently analyzed the effect of multiple normal coordinates on the corresponding transitions of $Cr_2F_9^{-3}$ [62]. It is likely that the quartet state of *trans*-$CrCl_2(H_2O)_4^+$ is also offset along several coordinates, but for the present analysis the one-dimensional model developed for the two preceding sections is sufficient.

The absorption band shape was calculated for the unpolarized spectrum of $Cs_2CrCl_5 \cdot 4H_2O$ at 5 K using time-dependent theory in a similar way than for the $NiCl_2(H_2O)_4$ chromophore. Only the coupling between the ^2E_g (U) and $^4T_{2g}$ (U) (O_h labels) was taken into consideration. The large off-diagonal matrix element cou-

pling these two states is $-\zeta\sqrt{6}/\sqrt{5}$ [5,43]. The calculation involves the totally symmetric Cr–Cl stretching mode; the excited state vibrational frequency is assumed to be 286 cm^{-1}, identical to the ground state Raman frequency. The origin of the quartet state in the calculation was set to 13655 cm^{-1}, the value observed experimentally in emission at 5 K, as shown in Fig. 13. The spin–orbit coupling constant λ was set to 57 cm^{-1} (63% of the free ion value), as obtained from EPR measurements on $Cr(H_2O)_6^{3+}$ in alums [63], a value that was also used for ligand-field calculations on chromium(III) ions doped into oxides by Wood et al. [64]. All parameters in this model calculation are determined experimentally, except the excited state distortion ΔQ of the quartet state, which was adjusted to obtain a good agreement between experimental and calculated spectra. Parameter values are summarized in Tables 1 and 4. The calculated absorption intensity of the ^2E_g state using the model is in good agreement with the observed spectra. The calculated spectrum is shown as a dotted trace on Figs. 11 and 12.

6. *trans*-$CoCl_2(H_2O)_4$

6.1. $CoCl_2(H_2O)_4 \cdot 2H_2O$

The $CoCl_2(H_2O)_4 \cdot 2H_2O$ compound is isostructural to the nickel(II) analog [17,18]. The low-temperature polarized absorption spectra show many unusual bandshapes for forbidden and allowed bands. The cobalt(II) ion has a d^7 electron configuration and Kramer's degeneracy is expected for all states. The density of states in the visible part of the spectrum is very high (see Fig. 15), and effects of coupled states are important. The close proximity of coupled states with identical symmetry makes this region of the cobalt(II) spectra unsuitable for a quantitative analysis with our model, which involves only two coupled electronic states of different spin multiplicity. The electronic absorption spectra of the cobalt(II) compound in Fig. 15 show very rich electronic and vibronic structure, similar to the spectroscopic results obtained for complexes in the preceding sections.

6.2. Spectroscopic results

Three quartet bands are expected for cobalt(II) compounds in octahedral symmetry. The first one is seen in the near-infrared region of the spectrum, involving the $^4T_{2g}$ state (O_h symmetry), split into ^4E_g and $^4B_{2g}$ in the D_{4h} point group. The assignment of the other two quartet bands is uncertain. For a mixed water and chloride ligand sphere, the $^4A_{2g}$ and $^4T_{1g}$ (O_h) states should be near a crossing point. Ferguson and Wood [10] have reported the $^4A_{2g}$ (O_h) state to be at 16450 cm^{-1} ($^4B_{1g}$ in D_{4h}) and the $^4T_{1g}$ state (O_h), to be split into ^4E_g and $^4A_{2g}$ (D_{4h}) at 18600 and 22250 cm^{-1}, corresponding to the strong bands in Fig. 15.

The Raman spectrum of the $[CoCl_2(H_2O)_4]$ chromophore is very similar to the analogous nickel(II) compound [65], confirming that the two compounds are

isostructural. The comparison of frequencies in Table 2 shows that some vibrational frequencies are similar for metals with identical oxidation states. For example, the ratio $\nu_{(CoO)}/\nu_{(NiO)}$ is about 0.99 for the totally symmetric stretching metal water mode. These frequencies are significantly different for trivalent ions, as illustrated by the ratio $\nu_{(CoO)}/\nu_{(VO)}$, which is 0.71.

We carried out single crystal EPR and magnetic susceptibility measurements in order to determine the zero field splitting of the ground state. In both experiments, exchange effects dominate at low temperature and it is not possible to determine energy levels for an individual complex in the concentrated crystal.

6.3. Effects of spin–orbit coupling between multiple states and vibronic transitions involving OH modes

The cobalt(II) ion with its d^7 electron configuration has the same 120 microstates as chromium(III). In the D_{4h} point group, a large number of doublet and quartet states are expected between 15000 and 30000 cm^{-1}. Numerous ligand field calculations have been reported for cobalt(II) complexes, supported by magnetic susceptibility and heat capacity measurements [66–69]. Four spectroscopic publications on $CoCl_2(H_2O)_4{\cdot}2H_2O$ include ligand field calculations, three of these in tetragonal symmetry [9–11] while one uses octahedral symmetry [12]. Due to the complexity of the absorption spectrum, the assignment of the bands is problematic

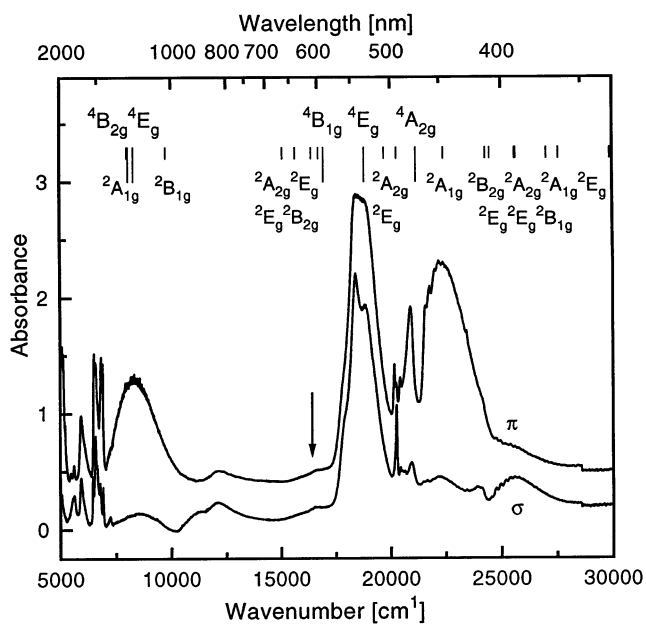

Fig. 15. Polarized absorption spectra of $CoCl_2(H_2O)_4{\cdot}2H_2O$ at 5 K. The vertical lines represent the AOM energies calculated with parameters from Table 2 with $\zeta = 0$. The tall lines represent spin-allowed transitions, the short lines the spin-forbidden transitions.

and there are substantial differences between the assignments given by different authors.

We are particularly interested in tetragonal symmetry and for that reason we have compared our spectra and analyses to those of Ferguson and Wood [10] and Joy and Fogel [11]. The main differences between the assignments in these two publications concern the splitting of the ground state and the splitting of the first excited state in the NIR. The literature assignments are in agreement for the complicated part of the spectrum between 15000 and 30000 cm^{-1}. Joy and Fogel [11] assign the first NIR transition to the $^4B_{2g}$ state at 6600 cm^{-1} while Ferguson and Wood [10] assign the first transition as ^4E_g at 8060 cm^{-1}. In Table 2 we use the value of Ferguson and Wood because there is no experimental evidence for a d–d transition at 6600 cm^{-1}, as this region is dominated by water overtones. Ferguson and Wood [10] found magnetic dipole zero phonon lines in the NIR located at 7092 and 7018 cm^{-1} (for $CoCl_2(H_2O)_4 \cdot 2H_2O$) and at 7122 and 7052 cm^{-1} (for $CoCl_2(D_2O)_4 \cdot 2D_2O$). These results show that an electronic transition located at 6600 cm^{-1} (below the electronic origins) is unlikely. The comparison to the water overtones in the spectra of the nickel(II) analog shows that both spectra are very similar in that region, as illustrated in Fig. 3. It is well known that nickel(II) aquo compounds have no electronic transitions at these low energies.

A peculiarity of this spectrum is the transition to the $^4B_{1g}$ (D_{4h}) state ($^4A_{2g}$ in O_h). In two reports [10,11], the authors locate it at approximately 16450 cm^{-1}, as denoted by the arrow in Fig. 15. At first sight, the transition seems to be weak for an allowed band but the electron configuration of its final state is $t_{2g}^3e_g^4$ and the intensity for such a two-electron excitation is expected to be low. For the $^4B_{1g}$ (D_{4h}) state of the cobalt(II) complex there is no strong coupling possible with states arising from other crystal field or charge transfer electronic configurations. The charge transfer bands of the cobalt complex occur at energies higher than 40000 cm^{-1}. This energy difference of more than 25000 cm^{-1} greatly reduces the efficiency of coupling, and intensity borrowing. It is interesting to note that none of the spin-allowed crystal field bands is particularly weak for the nickel(II) complex in Fig. 1, despite the fact that the $t_{2g}^4e_g^4$ configuration, corresponding to a two electron excitation, contributes to the $^3T_{1g}$ states. We have shown with ab initio calculations that these states arise from strongly mixed $t_{2g}^5e_g^3$ and $t_{2g}^4e_g^4$ configurations [70] and that therefore no unperturbed double excitations can be observed, in contrast to the cobalt complex in Fig. 15.

AOM calculations confirm the assignment of the $^4B_{1g}$ (D_{4h}) state. It is calculated at 16954 cm^{-1} with AOM parameters not too far from those of the related nickel(II) complex, as seen from Table 2. From magnetic susceptibility and heat capacity measurements, the position of the first two Kramer's doublets above the lowest energy state have been estimated at 152 and 630 cm^{-1} [67]. We were able to approximately reproduce the position of these doublets at 167 and 868 cm^{-1}.

The NIR part of Fig. 15 shows two maxima, the first one above 8000 cm^{-1} while the second is located near 12000 cm^{-1}. In π polarization, the first maximum is more intense than the second one. In octahedral symmetry, two states of different multiplicity are expected in this region of the spectrum, a $^4T_{2g}$ and a ^2E_g state. With

aquo and chloro ligands, these two states should have potential energy surfaces with a crossing point near the Frank–Condon region and strong effects of coupling on the spectrum can be expected. The electronic configuration for the $^4T_{2g}$ state is $t_{2g}^4e_g^3$ while it is $t_{2g}^6e_g^1$ for the ^2E_g state. This difference of two electrons between the two configurations leads to a value of zero for the spin–orbit coupling matrix element. The only quartet which can couple to this ^2E_g state is the ground state. Strong spin–orbit interaction between excited electronic states of different spin multiplicity can arise only in the visible part of the spectrum, in Fig. 15, for this cobalt(II) complex. Due to the high density of states that can interact in that spectral region, our simple model implying only two coupled states is inaccurate for a quantitative analysis of the spectrum. To avoid misuse of our model it is useful to remember the selection rules for spin–orbit coupling between states: the electronic configurations should not differ by more than one electron, the product of $\Gamma_1 \times \Gamma_2$ should contain T_1 (for the O point group) and the spin difference $\Delta S = 0, \pm 1$ [43]. The intensity of the weak ^2E_g band ($t_{2g}^6e_g^1$) in π polarization is therefore mostly borrowed from the $^4T_{1g}$ ($t_{2g}^5e_g^2$) ground state, the matrix element with all other quartets ($t_{2g}^4e_g^3$ and $t_{2g}^3e_g^4$) should be zero to respect the first selection rule.

The σ polarized transition between 25000 and 27000 cm^{-1} shows a vibronic progression with an interval of about 200 cm^{-1}. This frequency is observed in the Raman spectrum, as seen from Table 2. We found two strong bands at 183 and 199 cm^{-1}, in agreement with a literature study [65]. Ferguson and Wood [10] have discussed this transition in terms of an anomalous band. The position of the band shifts to lower energy upon deuteration, and it appears that an OH vibrational mode is involved in the transition, a situation similar to the first triplet band of the vanadium(III) complex discussed in Section 4.3. Weak bands involving OH modes are observed for nickel(II) aquo complexes [1,24] and for the chromium(III) complex [7]. Fig. 16 shows a comparison of this vibronic effect for all complexes. From this figure it is easy to see that all complexes discussed in this paper exhibit a transition similar to the band of the cobalt(II) compound. The vanadium(III) complex shows the most dramatic effect, its anomalous band is stronger than the normal band in σ polarization. The origin of the vanadium(III) side band has been discussed in detail in Section 4.3, testing several hypothesis that could also be considered for the other spectra in Fig. 16. The vibronic band is σ polarized for all complexes, except for $NiCl_2 \cdot 6H_2O$, and its intensity varies from very weak to strong. This comparison illustrates the subtle characteristics of the metal-centered d–d transitions of the title complexes, which provide detailed information on aspects of the electronic structure extending beyond the metal–ligand bonds.

7. Conclusion

Intersystem crossing effects are observed in the spectra of many transition metal complexes. The title complexes show several different manifestations of intersystem

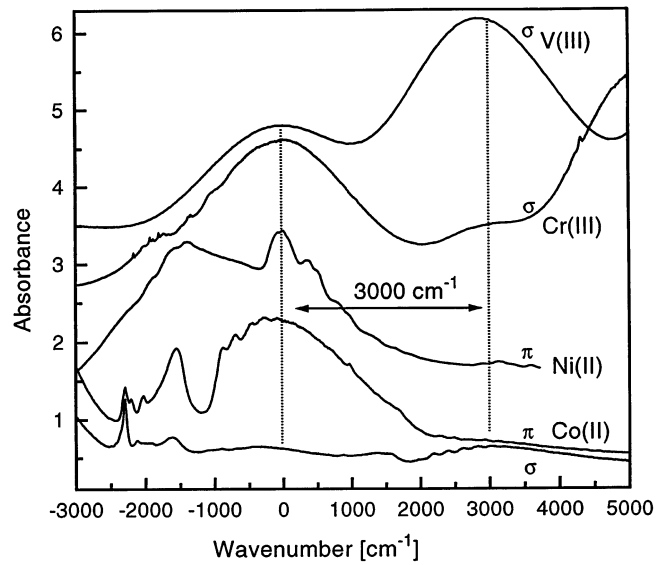

Fig. 16. Absorption spectra of *trans*-dichlorotetraaquo complexes showing the OH vibrations, from top to bottom: $Cs_3VCl_6{\cdot}4H_2O$, $Cs_2CrCl_5{\cdot}4H_2O$, $NiCl_2{\cdot}6H_2O$ and $CoCl_2{\cdot}6H_2O$. The maxima of the transitions of interest were set to 0 cm^{-1} for this comparison. Each spectrum shows a second maximum near 3000 cm^{-1}, corresponding to a vibronic transition involving a high-frequency OH mode.

crossings in their spectra. The sources of coupling are numerous and often hard to identify, but spin–orbit coupling always affects the band shapes and transition energies. The effect of spin–orbit coupling can be small and the forbidden bands can be hard to detect, like in the vanadium(III) complexes, or the effect can be drastic, increasing the vibronic interval in the spectra and the intensity of the formally forbidden transition, as observed for the nickel(II) complex.

Our calculations show that a simple model based on two coupled states allows us to quantitatively characterize the effects of intersystem crossing in many spectra. The calculated intensity ratios $I_{\text{allowed}}/I_{\text{forbidden}}$ vary by three orders of magnitude and are in good agreement with the experimental observations. Our model illustrates the relationship between ligand field theory (AOM) and vibronic effects involving potential energy surfaces. These two aspects have to be unified for a comprehensive and meaningful description of electronic states of transition metal complexes.

Acknowledgements

We thank Philip W.L. Tregenna-Piggot (Universität Bern) for the crystals of $CsAl(SO_4)_2{\cdot}12D_2O$: $V(D_2O)_6^{3+}$ and for help with the EPR measurements and Dominique Luneau (CEA Grenoble) for help with the magnetic measurements.

This work was supported by grants from the Natural Sciences and Engineering Research Council (Canada).

References

[1] G. Bussière, C. Reber, J. Am. Chem. Soc. 120 (1998) 6306.
[2] K. Jørgensen, Acta Chem. Scand. 9 (1955) 405.
[3] M.H.L. Pryce, G. Agnetta, T. Garofano, M.B. Palma-Vittorelli, M.U. Palma, Philos. Mag. B 10 (1964) 477.
[4] A. Lempicki, L. Andrews, S.J. Nettel, B.C. McCollum, E.I. Solomon, Phys. Rev. Lett. 44 (1980) 1234.
[5] R. Reisfeld, C.K. Jørgensen, Struct. Bonding (Berlin) 69 (1988) 63.
[6] U.R. Rodríguez-Mendoza, V.D. Rodríguez, V. Lavín, I.R. Martín, P. Nuñez, Spectrochim. Acta Part A 55 (1999) 1319.
[7] P.J. McCarthy, J.C. Lauffenburger, P.M. Skonezny, D.C. Rohrer, Inorg. Chem. 20 (1981) 1566.
[8] P.J. McCarthy, J.C. Lauffenburger, M.M. Schreiner, D.C. Rohrer, Inorg. Chem. 20 (1981) 1571.
[9] J. Ferguson, J. Chem. Phys. 32 (1960) 533.
[10] J. Ferguson, T.E. Wood, Inorg. Chem. 14 (1975) 184.
[11] W.H. Joy, N. Fogel, J. Phys. Chem. 79 (1975) 345.
[12] R. Pappalardo, Philos. Mag. B 4 (1959) 219.
[13] J. Gieleßen, Ann. Phys. 5 (1935) 537.
[14] E.J. Heller, Acc. Chem. Res. 14 (1981) 368.
[15] C. Reber, J.I. Zink, Comments Inorg. Chem. 13 (1992) 177.
[16] J.I. Zink, K.S. Kim Shin, Adv. Photochem. 16 (1991) 119.
[17] J. Mizuno, J. Phys. Soc. Jpn 16 (1961) 1574.
[18] J. Mizuno, J. Phys. Soc. Jpn 15 (1960) 1412.
[19] S.M. Horner, S.Y. Tyree, Inorg. Chem. 3 (1964) 1173.
[20] L.P. Podmore, P.W. Smith, Aust. J. Chem. 25 (1972) 2521.
[21] B. Morosin, Acta Crystallogr Sect. C: Cryst. Struct. Commun. 21 (1966) 280.
[22] I.G. Dance, H.C. Freeman, Inorg. Chem. 4 (1965) 1555.
[23] M. Magini, J. Chem. Phys. 73 (1980) 2499.
[24] E.I. Solomon, C.J. Ballhausen, Mol. Phys. 29 (1975) 279.
[25] S.P. May, H.U. Güdel, J. Lumin. 46 (1990) 277.
[26] S.P. May, H.U. Güdel, Chem. Phys. Lett. 164 (1989) 612.
[27] M. Kozielski, I. Pollini, G. Spinolo, J. Phys. C: Solid State Phys. 5 (1972) 1253.
[28] G. Benedek, I. Pollini, L. Piseri, R. Turbino, Phys. Rev. B 20 (1979) 4303.
[29] A. Bencini, C. Benelli, D. Gatteschi, Coord. Chem. Rev. 60 (1984) 131.
[30] M.A. Hitchman, R.G. McDonald, P.W. Smith, R. Stranger, J. Chem. Soc., Dalton Trans. (1988) 1393.
[31] C.E. Schäffer, Struct. Bonding (Berlin) 5 (1968) 68.
[32] K. Waizumi, H. Masuda, H. Ohtaki, K. Tsukamoto, I. Sunagawa, Bull. Chem. Soc. Jpn 63 (1990) 3426.
[33] M.D. Feit, J.A. Fleck, A.J. Steiger, J. Comput. Phys. 47 (1982) 412.
[34] J. Alvarellos, H. Metiu, J. Chem. Phys. 88 (1988) 4957.
[35] X.-P. Jiang, R. Heather, H. Metiu, J. Chem. Phys. 90 (1989) 2555.
[36] V. Engel, R. Schinke, S. Hennig, H. Metiu, J. Chem. Phys. 92 (1990) 1.
[37] D. Neuhauser, T.-J. Park, J.I. Zink, Phys. Rev. Lett. 85 (2000) 5304.
[38] P.L.W. Tregenna-Piggott, S.P. Best, H.U. Güdel, H. Weihe, C.C. Wilson, J. Solid State Chem. 145 (1999) 460.
[39] R. Meier, M. Boddin, S. Mitzenheim, V. Schmid, T. Schönherr, J. Inorg. Biochem. 69 (1998) 249.
[40] T. Schönherr, V. Schmid, R. Meier, Spectrochim. Acta Part A 54 (1998) 1659.

[41] R.S. Armstrong, A.J. Berry, B.D. Cole, K.W. Nugent, J. Chem. Soc., Dalton Trans. (1997) 363.
[42] J.T. Hougen, J. Mol. Spectrosc. 13 (1964) 149.
[43] J.S. Griffith, The Theory of Transition-Metal Ions, Cambridge University Press, Cambrige, 1961.
[44] T.W. Bitner, J.I. Zink, J. Am. Chem. Soc. 122 (2000) 10631.
[45] C.J. Ballhausen, Theor. Chim. Acta 3 (1965) 368.
[46] M.D. Sturge, Solid State Phys. Adv. Res. Appl. 20 (1967) 91.
[47] A.D. Liehr, J. Phys. Chem. 67 (1963) 389.
[48] H.C. Longuet-Higgins, U. Öpik, M.H.L. Pryce, R.A. Sack, Proc. R. Soc. Lond. Ser. A 244 (1958) 1.
[49] R.L. Carlin, C.J. O'Connor, S.N. Bhatia, Inorg. Chem. 15 (1976) 985.
[50] K. Kurzak, Spectrochim. Acta Part A 47 (1991) 1041.
[51] G.J. Goldsmith, F.V. Shallcross, D.S. McClure, J. Mol. Spectrosc. 16 (1965) 296.
[52] F.D. Camassei, L.S. Forster, J. Chem. Phys. 50 (1969) 2603.
[53] H. Riesen, L. Dubicki, Inorg. Chem. 39 (2000) 2206.
[54] J. Ferguson, H.J. Guggenheim, D.L. Wood, J. Chem. Phys. 54 (1971) 504.
[55] H.U. Güdel, T.R. Snellgrove, Inorg. Chem. 17 (1978) 1617.
[56] H. Riesen, E. Krausz, L. Dubicki, J. Lumin. 44 (1989) 97.
[57] K.K. Chatterjee, L.S. Forster, Spectrochim. Acta Part A 20 (1964) 1603.
[58] L.J. Andrews, A. Lempicki, B.C. McCollum, J. Chem. Phys. 74 (1981) 5526.
[59] L.S. Forster, Chem. Rev. 90 (1990) 331.
[60] A.D. Kirk, Chem. Rev. 99 (1999) 1607.
[61] B. Šopotrajanov, V. Stefov, M. Žugic, V.M. Petruševski, J. Mol. Struct. 482–483 (1999) 109.
[62] R. Schenker, M. Triest, C. Reber, H.U. Güdel, in press.
[63] A. Abragam, Resonance Paramagnetique Electronique Des Ions De Transition, Presses Universitaires de France, 1971.
[64] D.L. Wood, J. Ferguson, K. Knox, J.F. Dillon Jr., J. Chem. Phys. 39 (1963) 890.
[65] D.M. Adams, P.J. Lock, J. Chem. Soc., Dalton Trans. (1971) 2801.
[66] H. Taiichiro, J. Phys. Soc. Jpn 15 (1960) 483.
[67] N. Uryû, J. Skalyo, S.A. Friedberg, Phys. Rev. A 144 (1966) 689.
[68] B.N. Figgis, M. Gerloch, J. Lewis, F.E. Mabbs, G.A. Webb, J. Chem. Soc., Dalton Trans. (1968) 2086.
[69] M. Gerloch, P.N. Quested, R.C. Slade, J. Chem. Soc., Dalton Trans. (1971) 3741.
[70] J. Landry-Hum, G. Bussière, C. Daniel, C. Reber, in press.